

Thermal Infrared Imaging and Spectroscopy of Comet Hale-Bopp (C/1995 O1)

T. L. Hayward

Center for Radiophysics and Space Research, Cornell University, Ithaca, NY 14853

hayward@astrosun.tn.cornell.edu

M. S. Hanner and Z. Sekanina

Jet Propulsion Laboratory, California Institute of Technology

4800 Oak Grove Dr., Pasadena, CA 91109

msh@scn1.jpl.caltech.gov, zs@sek.jpl.nasa.gov

ABSTRACT

We present $\lambda = 3\text{--}5$ and $8\text{--}13\text{ }\mu\text{m}$ images and long-slit spectra of comet Hale-Bopp (C/1995 O1) taken in February–April 1997, near the time of perihelion passage. In agreement with other infrared observations, we find that the $3\text{--}13\text{ }\mu\text{m}$ spectral energy distribution was dominated by a $10\text{ }\mu\text{m}$ silicate feature with a strong underlying continuum. In the nuclear region, the feature's peak flux-to-continuum ratio varied from 2.8 on February 17 to 3.3 on April 19, and the color temperature of the $3\text{--}5\text{ }\mu\text{m}$ continuum was ~ 1.8 times the blackbody temperature. Both quantities are larger than in any previous comet and indicate a high abundance of submicron dust particles. Spectral structure within the silicate feature reveals the presence of crystalline olivine and pyroxene grains.

The physical properties of the grains, as evidenced by their infrared emission, correlated with the morphology. Within the visible jets and halos the silicate feature was up to 15% stronger, and the $8\text{--}13\text{ }\mu\text{m}$ color temperature ~ 1.1 times higher, than in the regions between the halos. Therefore, the halos were enriched in submicron particles relative to the background, as expected from the higher outflow velocities of these small grains. Within the halos, there was no measureable variation in the strength of the silicate feature or the color temperature with distance from the nucleus; that is, we detect no time-dependent evolution of dust particle properties (such as fragmentation) on a time scale of one rotational cycle (between ~ 2 and 13 h after ejection). The spectral shape of the silicate feature was essentially the same everywhere in the inner coma in all of our 1997 spectra.

Monte Carlo simulation of dust particle motions in the coma indicates that the observed patterns of jets and halos were dominated by submicron-sized grains. Modeling of the thermal emission from small grains demonstrates that the principal features of the $3\text{--}13\text{ }\mu\text{m}$ continuum and the $8\text{--}13\text{ }\mu\text{m}$ silicate feature can be synthesized from a mixture of amorphous carbon and amorphous and crystalline silicates.

The overall shape of the silicate feature resembled that in other bright comets, indicating a similar mineral mix. However, the $10.0\text{ }\mu\text{m}$ peak was sharper in Hale-Bopp near perihelion than in any previously observed comet except comet Mueller (C/1993 A1) at 2 AU.

Subject headings: comets: individual (Hale-Bopp C/1995 O1) – comets: general – mineralogy – interplanetary medium – interplanetary dust particles

1. Introduction

Comets are among the most pristine members of the solar system. Due to limited exposure to solar heating, the ice and dust in their nuclei probably have not been significantly altered since the nuclei were formed. Study of comets can therefore provide insight into the physical conditions of the early solar system.

Dust particles are an important component of most comets, and the infrared (IR) emission from grains heated by solar radiation is diagnostic of the grain size, composition, and albedo. Narrow-band photometric measurements in the $\lambda = 1\text{--}20\ \mu\text{m}$ IR bands accessible from the ground (e.g., Gehrz & Ney 1992) have shown that most cometary spectral energy distributions (SED) have a blackbody-like continuum with a color temperature T_c significantly higher than the equilibrium blackbody temperature at a given heliocentric distance. In many comets, broad emission features centered at $\lambda \sim 10$ and $20\ \mu\text{m}$ are detected above the continuum (e.g., Hanner, Lynch, & Russell 1994b). These features are attributed to silicate grains of radius $a \lesssim 1\ \mu\text{m}$. During comet Halley's apparition in 1986, IR spectrometers first detected an $11.2\ \mu\text{m}$ peak within the silicate feature that was attributed to Mg-rich olivine (Bregman et al. 1987; Campins & Ryan 1989). The $11.2\ \mu\text{m}$ feature has since been detected in several additional comets (e.g., Hanner et al. 1994a,b). Studies of interplanetary dust particles (IDPs) collected in the stratosphere indicate that cometary dust particles are aggregates of grains of $\sim 0.1\ \mu\text{m}$ diameter made up of crystalline and amorphous silicate and amorphous carbonaceous material (e.g., Bradley, Humecki, & Germani 1992; Bradley et al. 1999), in good agreement with the ground-based observations.

Comet Hale-Bopp (C/1995 O1) was discovered at heliocentric distance $r_h = 7.2\ \text{AU}$, more than 20 months before it reached perihelion on 1997 April 1. Its great intrinsic brightness, early discovery, and small perihelion distance provided a rare opportunity to observe a comet's evolution through a wide range of heliocentric distance and thus solar heating. The comet's brilliance was evidently due to the high mass loss rate from its large, 40–70 km diameter (Weaver & Lamy 1999; Sekanina 1999; Fernández et al. 1999a) nucleus and the high dust

content of its ejecta. Much of the dust was emitted in jets by a number of active sources on the nucleus. Between 1997 February and May, the periodic appearance of jets and the uniform spacing of the resultant halos indicated an $\sim 11.3\ \text{h}$ nuclear rotation period (Jorda, Lecacheux, & Colas 1997; Sarmecanic et al. 1997; Schleicher et al. 1998; Licandro et al. 1998), and permitted modelling of the nuclear spin axis orientation and the surface location of an active source (Sekanina 1998a). More detailed models of the jet activity are under development as the large database of images is more thoroughly analyzed.

Hale-Bopp was extensively studied in the infrared. Early spectroscopic observations made in 1996 May by the Infrared Space Observatory (ISO) (Crovisier et al. 1996) and in 1996 June at Palomar (Hayward & Hanner 1997) both detected surprisingly strong $10\ \mu\text{m}$ silicate emission even at the large heliocentric distances of $r_h = 4.6$ and $4.2\ \text{AU}$, respectively. This was the first time that strong silicate emission, indicative of submicron particles, had been seen at a distance where the blackbody temperature ($T \sim 130\ \text{K}$) is well below the sublimation temperature of water ice. At that temperature, we had expected that the small silicate grains and dark carbonaceous material would still be frozen inside larger icy aggregates. A prominent $11.2\ \mu\text{m}$ olivine peak was also visible in these early spectra. Additional ISO spectra taken in 1996 October at $r_h = 2.9\ \text{AU}$ displayed 5 sharp peaks of Mg-rich crystalline olivine between 16 and $34\ \mu\text{m}$ (Crovisier et al. 1997), confirming the previous identification of the $11.2\ \mu\text{m}$ peak. Ground-based photometry taken closer to perihelion revealed a very high color temperature and strong silicate feature that indicated an unusually high abundance of submicron grains (Williams et al. 1997; Mason et al. 1999). 8– $13\ \mu\text{m}$ spectra were taken by several groups in 1996 and 1997. All of these spectra consistently show structure in the silicate emission feature that can be attributed to pyroxene, as well as olivine, grains (Russell et al. 1997; Hanner et al. 1999; Galdemard et al. 1999; Wooden et al. 1999).

In this paper we present observations of Hale-Bopp at $\lambda = 3\text{--}18\ \mu\text{m}$ made with a modern 2-D array camera/spectrograph at the Palomar 5-m Hale telescope. The brightness of the comet and the use of a large telescope and advanced instrumentation

has resulted in a unique set of high signal-to-noise mid-IR images and spatially resolved spectra that elucidate the grain properties in the inner coma. The jets and halos seen in the optical are also easily visible in the mid-IR, and our 2-D array permitted searches for spectral variations between the nucleus, jets, and diffuse regions of the coma. In addition, the long time span of our observations allowed study of the dust emission over a wide range of heliocentric distances. We describe the observations and data reduction in § 2, and present the observational results in § 3. Preliminary models of our images and spectra are developed in § 4. Our findings are compared with other Hale-Bopp data and with other comets in § 5.

2. Observations and Data Reduction

We observed Hale-Bopp using the 5-m Hale telescope at Palomar Observatory, with the SpectroCam-10 (SC-10) mid-IR imaging spectrograph (Hayward et al. 1993) mounted at the telescope's f/70 Cassegrain focus.¹ SC-10 utilizes a Boeing 128×128 pixel Si:As BIB array detector and can function as both a camera and a long-slit spectrograph. Using camera mode, we imaged Hale-Bopp through six OCLI silicate set, 1 μm bandpass filters centered from 7.9 to 12.5 μm , a 3.4 – 5.0 μm filter, and a 0.5 μm wide filter centered at 17.9 μm . The diffraction-limited point-spread function (PSF) size (full-width at half-maximum) at Palomar is 0''.253 at 5.0 μm , 0''.505 at 10.0 μm , and 0''.904 at 17.9 μm . In good seeing conditions the diffraction limit is achieved above $\sim 8 \mu\text{m}$, but image quality is seeing-limited below 8 μm . The SC-10 64 pixel diameter unvignetted field spans 16''4 at 0''.256 per pixel. We also used the low-resolution spectrograph mode to take 7.5–13.5 and 3.4–5.0 μm long-slit spectra through 1'' and 2'' wide by 16'' long slits. The spectral resolution is 0.10 μm with the 1'' slit ($R = \lambda/\Delta\lambda \approx 100$) and 0.20 μm with the 2'' slit ($R \approx 50$).

The observations reported here were made on 1997 February 17–19, March 24–28 and April 19 UTC, and represent a large fraction of the Hale-Bopp data we collected between June 1996 and

April 1997. Pre-perihelion results were described by Hayward & Hanner (1997), and summaries of the entire campaign were given by Hayward & Hanner (1999) and Hanner et al. (1999). A log of the observing runs covered by this paper is presented in Table 1. Because of the comet's proximity to the sun, all observations were made either in daylight or bright twilight. In February and April, we could not observe Hale-Bopp with the sun above the horizon because the observing geometry caused direct sunlight to shine on the telescope. In February, therefore, we acquired the comet within minutes of its rising above the 12° altitude limit of the telescope, and ceased observing at sunrise. On April 19 we observed for a short period after sunset. In March, however, because the comet transited north of zenith, we were able to use the observatory dome as a light shield and pick up the comet in mid-afternoon, once the sun dropped to a safe altitude. Therefore, the quantity and quality of the March data are significantly higher than the data from February and April.

Observing conditions were frequently very good for the observations: the sky was clear and the image quality was subarcsecond at $\lambda \sim 10 \mu\text{m}$. The exceptions were on February 19, when the seeing was 1–2'', and on March 26–27, when we observed through thin cirrus. The data taken shortly after opening the dome in March (before the dome air reached equilibrium with the outside afternoon air) were degraded by 1–2'' seeing, but data from later in the afternoon are nearly diffraction-limited.

Three types of imaging data were taken: multi-wavelength sets (or image "cubes") of a single 16''×16'' field to map the broadband SED near the nucleus, mosaics up to 45''×45'' in size through a few filters to record the morphology of a larger area of the inner coma, and single frames bracketing a spectrum to document the position of the spectrograph slit relative to the intensity peak and the jets and halos. A log of the image cubes and mosaics is given in Table 2. Because SC-10 can switch between modes in only a few seconds, we could use the imaging mode to navigate the inner coma in real-time, placing the narrow spectrograph slit at a desired location typically to $\pm 0''.5$ accuracy. This capability was especially important near perihelion, when all observations were made during bright twilight or broad daylight and

¹ Observations at Palomar Observatory were made as part of a continuing collaborative agreement between the California Institute of Technology, Cornell University, and the Jet Propulsion Laboratory.

the comet was often invisible on the TV guider. Because the comet was so bright, most individual imaging and spectral integrations were only one to two minutes in length, and multiwavelength image cubes and spectral sequences were completed in 5 to 10 minutes. Large mosaics required 10 to 15 minutes to complete.

Our Hale-Bopp spectral data are listed in Table 3. The spectra from 1997 February cover 8.0 – 13.4 μm in three overlapping segments (each spanning 3.0 μm); the wavelength range was limited by the 8.0 μm cutoff of the instrument's order sorting filter and by strong telluric emission which saturated the detector at the long wavelength end. In March, to extend the wavelength coverage below 8.0 μm , which is critical for a more accurate determination of the continuum level, we included a fourth spectral segment taken through the 1 μm bandpass filter centered at 7.9 μm , and a fifth segment through the 3–5 μm filter. Due to the low detector quantum efficiency and the low grating efficiency below 7 μm , the S/N of the 3–5 μm spectra are relatively low despite the comet's brilliance.

In February, we used standard IR chopping and beam-switching techniques to remove the sky background emission, chopping at 2–5 Hz with a 120'' amplitude in the N-S direction. The integration time of individual frames taken between nods was 10 s, and 4 to 8 such frames were typically taken per filter or spectral segment. In March, the integration times were similar, but we were concerned that the usual beam-switching technique would place one of the reference beams in either the tail or the bright complex of halos that existed to the south and west of the nucleus. We therefore set the reference chop beam 120'' or 150'' to the east of the main beam, and periodically nodded 150'' east, thus placing both beams off-source in the direction in which the comet's surface brightness decreased most rapidly. Subtracting the data from the two nod positions then removed residual telescope emission that was not canceled by the chop in the same manner as the usual beam-switching method, except that the comet was in the field 1/4 of the time instead of 1/2. Fortunately, Hale-Bopp was so bright that the low efficiency was not a serious handicap. With this technique, the nod amplitude did not have to match the chop to a fraction of a pixel (which is necessary to achieve the best image quality in com-

bined pairs of beam-switched images), an important benefit because guiding on the moving comet during daytime was so difficult.

The images and spectra were processed using a library of custom routines written for the Interactive Data Language (IDL) environment. The processing included co-adding individual frames of an integration, dividing by flat-field images, combining mosaic frames into a single image, and combining multiple spectral segments into a single 2-D spectral image. The data were flux-calibrated using images and spectra of the standard stars listed in Table 1. Magnitudes of these stars are listed in Table 4. The magnitudes were derived from UKIRT CGS-3 spectra taken by one of us (MSH) that were integrated across the filter bandpasses, and from selected IRTF photometry of the stars taken through the same filters. The zero-magnitude fluxes needed to convert magnitudes to physical units were taken from Cohen et al. (1992). Absolute spectra in both the 8–13 and 3–5 μm bands were constructed from model spectra of the primary standards α CMa and α Lyr (Cohen et al. 1992) and archival SC-10 ratio spectra of the observed and primary standards.

Because the comet was often observed at relatively high airmass and during daytime, bracketing observations of standards at identical airmass were usually not possible. For the images, airmass corrections could be derived from the available standard star data, but calibration spectra were not sufficiently stable to permit a direct extinction correction. Therefore, we corrected the spectra using atmospheric transmission models generated by ATRAN (Lord 1992). This technique generally yielded good results except near the short wavelength ($\sim 9.2 \mu\text{m}$) edge of the 9.5 μm ozone absorption feature, where the slope of the feature is so steep that the comet and standard star spectra must be aligned to a small fraction of a pixel for a proper calibration. In practice, grating drifts, instrument flexure, and the variation of the source position in the slit led to slight misalignments which significantly degraded many calibrated spectra near 9.5 μm .

Proper calibration of images taken through the 3–5 μm filter also posed a significant problem because the filter spans both the *L* and *M* atmospheric windows, which are separated by a deep telluric absorption gap, and the color difference

between the comet and standard star (α Tau) was very large. Using profiles of the atmospheric transmission and the comet and standard star emission, we calculated a color correction factor for the 3–5 μm image fluxes of ~ 1.2 at the mean wavelength of 4.2 μm , but comparison with our well-calibrated spectral data from 1997 March 27–28 indicated that the correction factor is actually about 1.4. Variation of the detector quantum efficiency and the grating efficiency probably account for the difference. We calibrated the 3–5 μm images using the correction factor of 1.4 to maintain consistency between the images and spectra.

3. Observational Results

3.1. Inner Coma Morphology

In this section we discuss the morphology visible in our IR mosaics of Hale-Bopp’s inner coma. The large field covered by the mosaics best shows positions of jets and halos at the time of our observations, which will aid in the interpretation of our image cube and spectral data.

Figures 1 and 2 display five mosaics taken in February, March, and April. For each epoch we show both the original mosaic and a version which has been divided by a $1/\rho$ gradient, where ρ is the radius from the flux peak on the plane of the sky. A constant, spherically symmetric outflow will result in a $1/\rho$ surface brightness gradient, so dividing by this gradient emphasizes irregularities in the outflow. The gradient image was synthesized beginning with a circularly-symmetric $1/\rho$ profile centered on the brightest comet pixel. This image was then convolved with an image of a bright standard star to account for the instrumental PSF, and multiplied by a scaling factor. The scaling factor was chosen so that the quotient in the region to the north and east of the nucleus, where there are no strong jets or halos and the surface brightness declines nearly as $1/\rho$, was near unity. (The precise scaling does not affect the appearance of the figures.) In the February $1/\rho$ -divided images (Fig. 1), the surface brightness in the halos is up to 1.2 times the level between the halos. In the three March and April images (Fig. 2), the peak halo surface brightness is consistently 1.6 – 1.7 times the nearly constant level between the halos.

In order to compare images and spectra taken over a period of a few days, we need to define

the corresponding nuclear rotational phase. The steady expansion of the halos in the coma permits a determination of the nuclear rotation period, assuming that the halos originate from a specific active area on the rotating nucleus. Our temporal coverage is poor, so we cannot independently determine the halo expansion rate and nuclear rotation period. Two studies, Licandro et al. (1998) and Schleicher et al. (1998), have derived a mean rotation period of 11.34 and 11.31 hr respectively, based on long series of optical and near-IR images.

The difference in rotation period between these two studies can be understood by recognizing that, although the “sidereal” period, P_{sid} , remains constant, the solar period, P_{sol} , defined by the time difference between two successive transits of the Sun across the same local meridian on the nucleus, depends on the spin axis orientation and the comet’s position in its orbit. With a spin axis similar to that defined by Sekanina (1998a), we derive $P_{\text{sid}} = 0.4700$ days, or 11.283 ± 0.003 h, from the mean P_{sol} in the specific time intervals employed in the above-mentioned studies. P_{sid} then determines P_{sol} for any epoch of our observations.

The jet structure in February can be explained by a single source at latitude $+55^\circ$ (Sekanina 1998a), which we will call “Source A.” However, this single source does not reproduce the multiple spiral halos that were visible during March and April (our Fig. 2; Schleicher et al. 1998; Licandro et al. 1998). A better match is obtained by adding a second “Source B” at latitude $\sim +5^\circ$ and preceeding Source A by $\sim 130^\circ$ in longitude. Source A was still active in March and April, but was by then in constant sunlight because the polar axis was pointed very close to the Sun. In a study of optical images of Hale-Bopp’s inner coma, Vasundhara & Chakraborty (1999) derived latitudes and relative longitudes for the multiple jet sources that are similar to our values.

For the present work, we define the quantity N_{rot} to be the number of nuclear rotations from time t_0 , the time of local midnight at Source A immediately preceding the start times on the first day of, respectively, our February, March, and April runs, as listed in Table 1. All midnight, sunrise, and sunset times that are relevant to our observations are listed in Tables 5 and 6. The corresponding value of N_{rot} is listed with each displayed image.

The appearance of the inner coma in the February thermal-IR images (Fig. 1) is remarkably similar to the optical images taken by Jorda et al. (1997) on February 28 and reproduced in Sekanina (1998a). A narrow linear jet extends nearly $5''$ due south in the February 17.539 image, then bends sharply to the west; nearly 48 h later, on February 19.530, the jet appears more diffuse (partly due to poor seeing). Farther south are several bands of ejecta emitted by the active region during previous rotations. According to our nuclear rotation model, the two February mosaics approximately correspond to 6:42 and 9:27 (referred to the time from sunrise at Source A) in Figure 1 from Sekanina (1998a). In the panels near these times, the comet's appearance is similar, although not identical, to the mid-IR images taken ~ 10 days earlier. This demonstrates that the nuclear rotation and the active regions were fairly regular and repeatable over periods of several days, with changes occurring gradually.

The three mosaics from March and April (Fig. 2) show spiral halos similar to optical and near-IR images taken during this time (Licandro et al. 1998). In all three mosaics the halos appear to be double, in agreement with the shorter wavelength data. According to our model, the nuclear spin axis was pointing nearly at the Sun in late March and made an angle of $\sim 40^\circ$ with the direction to the Earth; the rotation appeared counter-clockwise to us at this time. The complex halo structure is due to superposition of ejecta from Source A and Source B, as described in § 4.1.

The morphology revealed by the mosaics will be compared with the spectral information in § 3.5 and discussed in terms of the dust dynamics in § 4.1.

3.2. Inner Coma Spectral Energy Distribution

The multi-wavelength image cubes and long-slit, low-resolution spectra contain a wealth of photometric information. Examples of these data are presented in Figure 3. Each row contains a $\lambda = 10.3 \mu\text{m}$ image which is only $15'' \times 15''$ in size (a single SC-10 field — the corners are cut off due to the circular field stop in the camera), and is one of eight planes from the full image cube. The multi-filter photometry measured from the encircled regions is displayed as the open circles in the

right panels. The strong silicate feature that is a signature of comet Hale-Bopp is immediately obvious.

Also displayed in Figures 3a and 3b are low-resolution spectra extracted from the 2-D spectral images at the positions of the rectangles overlaid on the images. On March 25–26, the spectrum was taken using a $1''$ slit about 2 h before the image cube. On March 27–28 we used a $2''$ slit and the images and spectra were taken over a span of just 20 minutes. As described in § 2, bracketing quick-look images were used to determine the slit position on the comet, so the indicated slit positions are accurate to $\sim \pm 0''.5$.

The data plotted in Figure 3 demonstrate that the imaging photometry and the spectroscopy agree very well, which is significant because the imaging and spectral data were taken and calibrated independently. The good agreement of the two types of data minimizes the possibility that a number of observation and calibration problems, such as background shifts due to cirrus clouds or photometric variations due to periods of poor seeing, are leading to erroneous interpretations.

We have plotted two examples of photometry and spectra in Figure 3 to illustrate three important limitations of our data. The first is the difficulty of flux calibration near the deep telluric ozone absorption at $9.5 \mu\text{m}$ (see § 2). Figure 3a shows one of the best results in which both the comet and standard star data were taken at low airmass with a $1''$ slit. The narrow slit resolves the complicated ozone absorption enough to provide a good calibration, but there is still a small ripple at $9.50 \mu\text{m}$ that is almost certainly an artifact. Assigning large error bars to these points would be misleading because the calibration error is systematic and is not due to low signal-to-noise. Figure 3b exhibits a much larger ozone miscalibration which we attribute to a larger airmass difference and a $2''$ slit, which poorly resolves the ozone feature.

The second difficulty is that the spectral flux calibration becomes uncertain below about $8 \mu\text{m}$ due to the rapidly decreasing atmospheric transmission. In Figure 3a the spectrum appears to flatten out slightly at $8 \mu\text{m}$, as one might expect where the silicate feature blends into the underlying continuum, but in Figure 3b it continues to drop steeply to the last point. Due to such ambi-

guities, the 8–13 μm continuum color temperature values we derive are uncertain by about ± 5 K.

The final problem is the relative flux calibration between the 3–5 and 8–13 μm spectra. Because the segments don't overlap in wavelength, their individual absolute flux calibrations must be correct in order to determine the true 3–13 μm SED. Absolute flux uncertainties are high for 1'' slit data because even a 0''.1 – 0''.2 pointing drift during an integration can cause a 10 – 20% error, but 2'' slit data are much less sensitive. Note that the 3–5 μm segment appears significantly higher relative to the 8–13 μm data in Figure 3a (1'' slit) than in Figure 3b (2'' slit). Because of the wider slit and more stable calibration, we believe the SED indicated by Figure 3b is more reliable.

Despite these problems, the consistency between the spectra and the image cubes, and from day to day, give us confidence in the accuracy of the photometry and spectral features. Moreover, a comparison of SC-10 spectra with other spectra taken near perihelion by different instruments shows a very consistent spectral shape (Hanner et al. 1999).

The continuum emission from comets can be characterized by comparing the color temperature over a specified wavelength interval to the temperature of a black conducting sphere at the comet's heliocentric distance, r_h . This ratio, called the "superheat," is defined as

$$S(\lambda_1, \lambda_2) = \frac{T_c(\lambda_1, \lambda_2)}{T_{\text{BB}}} = \frac{T_c(\lambda_1, \lambda_2)\sqrt{r_h}}{278 \text{ K}}, \quad (1)$$

where $T_c(\lambda_1, \lambda_2)$ is the color temperature of the thermal-IR continuum between λ_1 and λ_2 , r_h is the heliocentric distance in AU, and T_{BB} is the blackbody temperature at r_h (see Table 1).

$S(\lambda_1, \lambda_2)$ must be interpreted carefully because T_c varies significantly with wavelength. Gehrz & Ney (1992) and Williams et al. (1997) calculate $S(3,5)$ from photometry at 3 and 5 μm , away from the silicate feature. Taking $T_c(3,5) \approx 520$ K on March 28, we find $S(3,5) \approx 1.79$, in good agreement with the value of 1.84 measured by Williams et al. (1997) on February 20. This value of S is considerably higher than in any other comet, and indicates that the dust particles in Hale-Bopp are unusually small (Williams et al. 1997).

3.3. Nucleus Flux

High angular resolution mid-IR images of several comets have revealed emission arising directly from the unresolved nucleus at the center of the coma (e.g., Lisse et al. 1999; Fernández, Lisse, & A'Hearn 1999b). In our Hale-Bopp images taken near perihelion, however, we find that the comet's intense dust production masked any signature of the nucleus. Figure 4a depicts an east-west cross section through the March 27.985 mosaic (Fig. 2b) at the declination of the nucleus. Profiles through a standard star image that represents the PSF, and the synthetic $1/\rho$ gradient image are also shown. The comet profile is much broader than the PSF. Figure 4b shows the observed comet flux divided by the $1/\rho$ curve. There is no sign of an unresolved component in these profiles.

Note that the $1/\rho$ -divided profile in Figure 4b is fairly constant (and near unity because of the choice of scaling factor) to the east of the origin. The profile begins to rise $\sim 1''$ east of zero offset, and peaks in the middle of the halo to the west. The rise slightly east of zero (the position of maximum intensity) is seen in all the mosaics and image cubes taken near perihelion, and could be due to slight misalignment of the observed and $1/\rho$ gradient images or strong asymmetric outflow very close to the nucleus. However, it may indicate that the nucleus does not lie at the position of maximum flux where we have set the origin of the coordinate system. The peak flux may actually be out in the jet.

3.4. Periodic Flux Variations

In Figure 5a we plot 7.9, 10.3 and 12.5 μm photometry from the March image cubes against the phase of the nuclear rotation. The fluxes were measured in a 4''3 diameter synthetic aperture centered on the intensity peak. Data from all the available image cubes and mosaics are plotted except for several from March 26–27 which were obviously corrupted by cirrus clouds. At all wavelengths, we find a 30% variation in flux that is correlated with the nuclear rotation. The flux is weakest near phase 0.5, which is $\sim 1/2$ h after sunset at Source B according to our rotation model; see Table 6. At Source B sunrise (phase 0.84) the nuclear flux is in the midst of a steady increase. Therefore, we may have detected the modulation

in jet activity from Source B in the immediate vicinity of the nucleus. The variation could be partly due to changing seeing (which tended to improve gradually from early to late afternoon), or an incorrect airmass correction, but Figure 5a clearly shows that Hale-Bopp did not exhibit large, random outbursts during the period of our observations. The variation we may have detected is much smaller than the fluctuations in the thermal-IR luminosity of comet Halley (Gehrz & Ney 1992; Gehrz et al. 1995).

It is also of interest to look for relative variations between the three different wavelengths plotted in Figure 5a, which might indicate changes in the average grain size distribution or optical properties as the jets turn on and off. We computed $T_c(8,13)$ from the 7.9 and 12.5 μm points to evaluate the continuum. These filters extend into the wings of the silicate feature, but comparison with spectra indicates that the flux ratio between the filters is more strongly influenced by the continuum than the feature. To evaluate the silicate feature strength, we define \mathcal{R} as the ratio between the observed 10.3 μm flux and $B(10.3 \mu\text{m}, T_c)$. In Figure 3, for example, $T_c(8,13) \approx 400 \text{ K}$, and $\mathcal{R} \approx 2.6$.

The $T_c(8,13)$ and \mathcal{R} values derived from the photometry are plotted in Figures 5b and 5c. We do not see a definite periodic variation in these parameters. The continuum and silicate feature fluxes vary by a similar amount, and although we cannot rule out small relative changes, we do not see effects such as the silicate feature changing in strength while the continuum remains nearly constant.

What do our spectra show? Figure 6 displays several 8–13 μm spectra of the nuclear region from all four days of the March run, covering nearly the same range in rotation phase (0.51 to 0.02) as the image cube data plotted in Figure 5. Reliable absolute fluxes cannot be extracted from these narrow-slit data because of pointing and seeing effects, so the plotted spectra are normalized to an intensity of 10.0 at $\lambda = 12.8 \mu\text{m}$. However, we can look for relative changes in the continuum and silicate feature. The shape of the silicate feature and $T_c(8,13)$ are essentially identical in all spectra. The \mathcal{R} values derived from the spectra, plotted as asterisks in Figure 5c, vary by about 10%, but again the variation appears to be random and not

obviously correlated with the rotation phase and the activation of Source B near phase 0.84.

The steadiness of $T_c(8,13)$ and \mathcal{R} indicates that the activation of Source B near phase 0.84 may result in an increase in the number of particles near the nucleus, but does not strongly affect the average size distribution or optical properties of the grains.

3.5. Spatial Variation of Dust Optical Properties

Our image cubes and spatially resolved spectra allow us to investigate whether the optical properties of dust particles vary with position in the coma. We focus on two parameters related to the size and composition of the grains which can be defined easily from our data: the color temperature of the continuum and the strength of the silicate feature. These parameters can be mapped across our images, allowing us to look for any correlations between the morphology and the dust properties.

3.5.1. Image Cubes

Photometry from three different regions of the March 28.037 image cube are plotted in Figure 7. The strength of the silicate feature varies between the nuclear region, the curved jet, and an area just behind the jet (regions A, B, and C, respectively). The feature is about 13% stronger in the jet than in region C. In addition, the 3–5 μm flux is 23% higher relative to the 13 μm continuum in the jet than in region C. Both observed variations can be interpreted as a change in the mean grain size between the jet and other regions in the coma.

To investigate the spatial variations more thoroughly, we calculated $T_c(8,13)$ and the silicate flux-to-continuum ratio \mathcal{R} defined in § 3.4 pixel-by-pixel for each image cube. The results for 8 cubes are shown in Figures 8 and 9. The image cubes chosen for display were all taken in good seeing and clear weather, conditions which were critical for good spatial registration, background stability, and flux calibration. In good seeing, each of the images in a cube exhibited a well-defined flux peak that permitted registration of the planes to about 1 pixel (0''.25) accuracy. Each row of the two figures shows the 10.3 μm plane divided by $1/\rho$, and maps of the parameters $T_c(8,13)$ and \mathcal{R} . The 10.3 μm intensity isophotes are overlaid on

each panel to facilitate comparison of the parameter maps with the morphological features. The parameter values within $\sim 1''$ of the flux peak are sensitive to small registration errors and seeing variations between the image cube planes, so structure visible in this region should be disregarded. Outside the nuclear region the surface brightness variation is smoother and the parameter values are much less sensitive to misalignments.

One sees in Figures 8 and 9 that T_c and \mathcal{R} correlate and that they generally follow the jet patterns, rather than the total brightness isophotes. The two image cubes in Figure 8 were taken shortly before and after the February 17.539 mosaic (Fig. 1a). The westward-pointing arm of the jet expanded $\sim 2''$ to the south in the 1.66 h between the two image cubes. Both $T_c(8,13)$ and \mathcal{R} peak near the tip of the jet at the western edge of the image. The regions of high T_c and \mathcal{R} follow the jet arm as it expands to the south.

Figure 9 displays six image cubes taken during 1997 March. The spiral jet is easily seen in the $1/\rho$ -divided images. Although there is clearly spatial structure in the T_c and \mathcal{R} , these parameters do not so closely follow the jet visible in the $1/\rho$ -divided images. These parameter values are high near the leading edge of the jet, but they are also high to the north of the nucleus, where there is no visible jet. The most prominent feature of the parameter maps is the minimum to the south, behind the visible jet. Figures 9e and 9f show the comet 2 to 4 h after sunrise at Source B, according to our rotation model (see Table 6). The new jet may be visible forming to the east of the nucleus.

We interpret the fact that T_c and \mathcal{R} vary with position to be an effect of differences in the mean grain size with position in the coma. The velocity imparted to the dust particles by the outflowing gas is higher for smaller particles, thus the micron-sized and smaller particles which give rise to a high color temperature and strong silicate feature will tend to be at the leading edge of the jets and halos. The effects of velocity sorting will be discussed in more detail in § 4.1.

3.5.2. Spectra

Our long-slit spectra confirm the temperature and silicate feature strength variations seen in the image cubes, and provide additional information

about the shape of the silicate feature. Figure 10 displays spectra of the nuclear region, jet, and coma on February 17 and 19, scaled to the $12.8 \mu\text{m}$ continuum to emphasize variations in the strength of the silicate feature. As with the images, we find that $T_c(8,13)$ and \mathcal{R} are both higher in the jet (regions C & D) than near the nucleus or in the diffuse part of the coma. The value of \mathcal{R} is $\sim 2.3 - 2.4$ in the nuclear region and $\sim 2.6 - 2.9$ in the jet, in good agreement with the image cube values. The $T_c(8,13)$ values are more difficult to compare because the spectra cut off at $8.0 \mu\text{m}$, but also appear to be in good agreement.

In Figure 11 we plot the intensity, $T_c(8,13)$, and \mathcal{R} along the lengths of the two slits shown in Figure 10b (February 19). The color temperature peaks weakly in the halo $7 - 8''$ S of the nucleus in both spectra. (The uncertainty is high because of the low S/N at the $8 \mu\text{m}$ end of the data, especially at large distances from the nucleus.) The silicate feature strength also peaks in the jet position in both spectra. It dips to a minimum at offset $\sim 12''$ S, then rises again in the next halo.

Do the dust optical properties change with time from ejection? During the March run we were able to explore this question by taking spectra of two successive halos at much different distances from the nucleus. In Figure 12a, the spectrum running north-south through the nuclear region and a region of the halo where the ejecta are seen only ~ 2 h after ejection (region B) again reveals that both $T_c(8,13)$ and \mathcal{R} peak in the halo. In Figure 12b, the full length of the same spectrum is overlayed on a large mosaic, showing that a similar peak is found in the previous halo (region E) which is ~ 13 h old. The silicate feature strength is also high in the jet at region F, but is relatively weak between the halos in regions C and D.

These observations suggest that there is no systematic change with time in the optical properties of dust particles in the halo itself, on a time scale of one rotation cycle (between approximately 2 and 13 h post-ejection). For example, if the silicate particles were initially covered by mantle material opaque at $10 \mu\text{m}$ that gradually sublimated, then one would expect the strength of the silicate feature to increase with time, contrary to the observation.

Figure 13 displays additional spectra from March 27–28 and April 19 that show similar pat-

terns of temperature and silicate feature variations. On March 27–28, region C in the jet close to the nucleus and D in a more distant halo exhibit very similar enhancements in both quantities relative to the nucleus region and regions between the halos, consistent with the results from March 24.95. Spectra E, F, and G verify the observation from the image cubes in late March that the silicate flux-to-continuum ratio was slightly higher to the north of the nucleus and spiral jet than in the jet itself.

3.6. Shape of the Silicate Feature

Our high signal/noise spectra reveal details of the spectral structure in the 10 μm Si-O stretching band caused by the mixture of minerals in the comet dust. In addition to the olivine features at 11.2 μm and 11.9 μm there is a broad peak at 10.0 μm , a distinct shoulder at 9.3 μm , and a possible weak feature at 10.55 μm . The silicate mineralogy will be discussed in § 4; here, we examine in more detail the temporal evolution of the silicate feature.

Figure 14 displays a subset of our spectral data to show the evolution of the 8–13 μm silicate feature and continuum with heliocentric distance. Each spectrum plotted here was taken through the 1" slit and at relatively low airmass so that the flux calibration through the 9.5 μm ozone feature is reliable. Most of the spectra cover the nucleus region, but we include two spectra of the jet from February 19.577 (region D from Fig. 10b) and March 24.947 (E from Fig. 12b). We also include three spectra from 1996 June, August, and September (Hayward & Hanner 1997).

Figure 15a displays each spectrum after dividing by the blackbody functions shown by the dotted lines in Figure 14. The blackbody color temperatures were chosen to place the flux/continuum curves near unity at ~ 7.8 and 12.8 μm , taking into account the fact that the silicate feature is still declining where many of the spectra stop at 8.0 μm . Figure 15b and c display *all* the flux/continuum spectra from panel (a) after the amplitude of the silicate feature has been normalized to equal 2.0 at 10.0 μm .

Figure 15a illustrates the large increase in the silicate feature strength as the comet approached and passed perihelion. The 10.0 μm flux-to-

continuum ratio \mathcal{R} in the nuclear region increased from 1.8 in 1996 June, when it was already as strong as in any other comet, to 3.3 by April 19. A flux-to-continuum ratio near 3.3 was also recorded in the jet on February 19, when the nuclear region ratio was ~ 2.8 .

Despite the increase in the overall silicate feature strength, Figure 15b reveals that *the relative strengths of the 10.0, 11.2, 11.9, and 9.3 μm features are identical within the observational uncertainties in every spectrum taken near perihelion.* This consistency indicates that there was little change in the grain mineralogy in the months near perihelion. Furthermore, the mineralogy of particles in jets and between jets must also be similar; the various silicate components producing the composite spectrum must be well mixed.

However, there does appear to be a change in the silicate feature shape as the comet approached the sun. The main 10 μm peak was quite broad and centered at 9.7 μm in 1996 June and August, while near perihelion there is a narrower 10.0 μm peak and the 9.3 μm shoulder is more clearly separated. The change in shape appears to have happened by late September when the peak and shoulder are clearly visible. The shoulder is also visible in the early October spectrum by Wooden et al. (1999).

3.7. Summary of Observations

Our observational results, including the 1996 data described by Hayward & Hanner (1997), can be summarized as follows.

1. The strong, rotating jet and expanding halos observed in reflected sunlight are easily visible in the thermal IR.
2. Despite the jet activity, we find evidence for only a $\sim 30\%$ periodic variation in the total thermal IR flux close to the nucleus during a 76 h period between March 24–28. The variation appears to be correlated with the activity of the near-equatorial Source B in our nuclear rotation model as it passes in and out of sunlight. Near the nucleus, the continuum color temperature and silicate feature strength do not exhibit similar periodic temporal variations.

3. Our $\lambda = 3\text{--}13\ \mu\text{m}$ spectra show a strong $10\ \mu\text{m}$ silicate feature at each observed epoch from 1996 June through 1997 April, in agreement with many other IR observations. The silicate feature flux-to-continuum ratio in the nuclear region was already 1.8 in 1996 June and increased to 3.3 by 1997 April.
4. The silicate feature in 1997 displayed distinctive olivine features at 11.2 and $11.9\ \mu\text{m}$, a peak at $\sim 10\ \mu\text{m}$, a shoulder near $9.3\ \mu\text{m}$, and possible structure near $10.5\ \mu\text{m}$. The relative strengths of these features were nearly constant from February through April, indicating a constant grain mineralogy.
5. The silicate feature in 1996 always exhibited the olivine features at $\lambda = 11.2$ and $11.9\ \mu\text{m}$. The 1996 June and August spectra show a broad maximum in the silicate feature at $9.7\ \mu\text{m}$, instead of the narrower $10\ \mu\text{m}$ peak.
6. The color temperature of the $3\text{--}5\ \mu\text{m}$ continuum emission was about 1.8 times the blackbody temperature on 1997 March 28, higher than observed in any other comet. The $8\text{--}13\ \mu\text{m}$ color temperature in the nuclear region increased from 1.31 times the blackbody temperature in 1996 June to 1.38 near perihelion.
7. The silicate feature was consistently stronger by 10–20% and $T_c(8,13)$ was higher by 20–40 K in the jet and halos than in neighboring regions of the outflow.
8. The $3\text{--}5\ \mu\text{m}$ continuum was also elevated in the jet and halo regions.
9. Our data show no systematic variation in the silicate feature strength or $T_c(8,13)$ that is correlated with distance from the nucleus either within the jets or outside the jets. Therefore, we do not detect any time-dependent evolution of dust particles as they flow outward from the nucleus on a time scale of one rotation cycle (between ~ 2 and 13 hours after ejection).
10. We also observe no variation in the relative strengths of the 11.2 , 10.0 , or $9.3\ \mu\text{m}$ features with time or with position in the coma

that might indicate differences in dust particle mineralogy.

4. Modeling

In order to investigate dust particle properties such as size distribution and composition in detail, we have begun to model our data with numerical methods. In this section we describe two techniques: Monte Carlo simulation of dust grain motions in the coma, and modeling of the $3\text{--}13\ \mu\text{m}$ spectra with a mixture of grain types. In the future we plan to combine these two approaches to reproduce the observed spatial and spectral variations in the inner coma.

4.1. Dynamical Modeling of the Coma Morphology

Our modeling of Hale-Bopp's morphology utilizes a Monte-Carlo simulation technique which computes the trajectories of dust particles emitted from discrete sources on a rotating nucleus (Sekanina 1996). The particle loci are calculated as a function of two parameters. The first is β , the ratio of the force of solar radiation pressure to the force of solar gravity, which for spherical particles is related to more fundamental grain properties by

$$\beta = \frac{0.574 Q_{\text{pr}}}{a\rho}, \quad (2)$$

where a is the radius (in μm) of the particle, ρ is its bulk density (in g cm^{-3}), and Q_{pr} is the efficiency factor for radiation pressure.

To determine β for specific grain types, we have calculated $Q_{\text{pr}}(a, \lambda)$ using Mie theory and the optical constants of amorphous carbon and glassy olivine (Edoh 1983; Dorschner et al. 1995). The $Q_{\text{pr}}(a, \lambda)$ were then integrated over wavelength, weighted by the solar flux (Burns, Lamy, & Soter 1979) to determine the mean Q_{pr} for each grain size and composition. As indicated by Equation 2, β also depends inversely on the particle size, which here is intended to represent the size of individual compact grains whether they are separated or in extremely fluffy aggregates. The maximum β achieved for $a \sim 0.1\text{--}0.2\ \mu\text{m}$ is $\beta_{\text{max}} > 1$ for absorbing carbon grains and $\beta_{\text{max}} \sim 0.5\text{--}0.6$ for dielectrics such as silicates.

The second parameter is the particle ejection velocity, v_{eject} , resulting from momentum transfer

by the outflowing gas in the immediate proximity of the nucleus (within ~ 20 nuclear radii). This velocity can be related to β by the empirical formula

$$v_{\text{eject}}^{-1} = A + B\beta^{-1/2}, \quad (3)$$

where A and B are parameters that depend on the nuclear size and the gas and dust emission parameters (Sekanina 1981; Sekanina & Larson 1984, 1986). From Equations 2 and 3 it follows that v_{eject} varies inversely as the square root of the grain size so that the smallest particles will tend to be at the leading edge of the expanding jets and halos.

For Hale-Bopp, we use $A = 1.6 \text{ s km}^{-1}$ and $B = 0.15 \text{ s km}^{-1}$ as estimated by Vasundhara & Chakraborty (1999) from their modeling of optical images of the inner coma. The value of B is much lower for Hale-Bopp than for comets such as Swift-Tuttle or Halley (Sekanina 1981; Sekanina & Larson 1984, 1986). The reason for this low value is the comet's large nuclear size, which, in turn, implies a slower lateral dispersion of the expanding gas with increasing distance and therefore a more efficient momentum transfer from gas to dust. Consequently, not only the smallest (submicron-sized) grains, but also particles up to a few microns in size will have high v_{eject} and will populate the expanding jets and halos, which represent the leading edge of the ejecta from the active areas on the nucleus. At an assumed density of 2.5 g cm^{-3} , for example, all particles with $\beta > 0.15$ (i.e., silicate particles up to $\sim 1.6 \text{ }\mu\text{m}$ radius) will have v_{eject} within 15% of the peak value of 590 m s^{-1} .

In our Monte Carlo simulations, the deterministic approach is modulated by the introduction of random digital noise (Sekanina 1991) which mimics both the inherent stochastic processes (such as vectorial dispersion of the expanding particle flow) and circumstantial effects (such as seeing). The model follows the dust particle motions over five nuclear rotations.

To illustrate how β and v_{eject} affect the coma morphology, we have computed synthetic images of Hale-Bopp for specific particle size ranges, using the nuclear rotation and source locations described in § 3. Figure 16 displays synthetic images to compare with our February images. The three columns represent the epochs of the February 17 images shown in Figures 1a and 8. Each

of the four rows refers to a different range of β for the cases of submicron carbon, submicron silicate, and two larger particle sizes. The ejection velocity decreases with increasing grain size according to Equation 3. The synthetic images show the particle distribution only and are not intended to depict the relative thermal emission between the grain types.

The effect of β can be seen in Figure 16 by comparing rows (a) and (b), which represent submicron absorbing carbon and dielectric silicate grains, respectively. The series of arcs corresponds to ejecta from successive nuclear rotation cycles. Although the grain sizes, hence v_{eject} , are similar, the spacing between the second and third arcs is more compressed in row (a) because the solar radiation pressure is more rapidly decelerating the carbon grains. The higher β of the absorbing grains also causes the west end of the arcs to slant towards the north more steeply. The influence of v_{eject} is evident from comparison of the bottom three rows, for which the radiation pressure deceleration is much smaller. The length of the jet to the west of the nucleus, as well as the spacing of the arcs, is larger for the smallest, fastest particles (row b) than for the $15 \text{ }\mu\text{m}$ and $20\text{--}50 \text{ }\mu\text{m}$ particles (rows c and d). The arcs for the silicate particles are more evenly spaced than for the absorbing particles, showing that the motions of these particles are dominated by their ejection velocities. The large *range* of v_{eject} used for row (d) causes the individual arcs to blur.

When we compare Figure 16 with the morphology of the $1/\rho$ divided mosaics in Figure 1, it is evident that the arcs in our mosaic more closely resemble the spacing and slant in row (b). That is, our data tend to favor particles with $\beta < 1$.

The examples shown in Figure 16 allow us to interpret qualitatively the salient features of Figure 8. The extension of the jet to the west contains the smaller, faster particles, consistent with the higher T_c and stronger silicate feature at the western edge of the image. The T_c , which is strongly influenced by small absorbing grains, and the silicate feature strength vary together, because in this near-nucleus region v_{eject} controls the morphology, and v_{eject} does not depend appreciably on the composition. Between February 17.515 and 17.584 the area of high T_c moved south, reflecting the expansion of the jet.

By late March, the coma exhibited quite a different, and more complex, pattern. Source A, at $+55^\circ$ latitude, is now circumpolar and a new region, Source B, at about $+5^\circ$ latitude, has become active (Tables 5 and 6). Figure 17 presents synthetic images for the epoch of 1997 March 28.037, corresponding to the image cubes in Figure 9e (compare also with Fig. 2b). The four rows in Figure 17 correspond to the same range of β as in Figure 16, and the effects of different v_{eject} and radiation pressure deceleration are again visible. The first column shows ejecta from Source A. Since the Sun was above the horizon of this source throughout the rotation cycle, our model predicts that the dust was emitted from it without interruption, in rather tight loops to the south of the nucleus. The tight inner spiral from this source is clearly seen in Figure 2b. The elevated T_c and silicate feature to the north of the nucleus in Figure 9e most likely arise from submicron sized particles ejected from Source A around midnight local time (when the Sun was more than 40° above the horizon).

The middle column of Figure 17 exhibits the distribution of ejecta from Source B and the right column shows the sum of the contributions from the two sources. Source B is obviously responsible for the less curved halos in Figure 2b, while the bifurcations of the halos (best seen to the south of the nucleus) are clearly explained by superposition of the ejecta from the two sources in projection onto the plane of the sky. The high T_c and silicate feature immediately to the east of the nucleus in Figure 9e correspond to the most recent ejecta from Source B as a new rotation cycle commences. By contrast, the high T_c and silicate feature to the west of the nucleus are due to the combined ejecta from Source A and Source B. The prominent minimum in T_c and \mathcal{R} in Figure 9 to the south of the nucleus is consistent with the “hole” within the spiral loop for the small particles (rows *a* and *b*).

As was the case in February, the halo pattern in Figure 17b more closely predicts the location of the second halo in Figure 9e, indicating that the main contribution to the thermal emission from the halos arises from particles with $\beta < 1$.

The computations presented in Figures 16 and 17 are illustrative only. They indicate the range of particle properties influencing the coma morphology. A full model for the dust coma must be integrated over a broad size distribution of grains and

explicitly account for the thermal emission from each grain size; this work is in progress.

4.2. Modeling the Spectra

In this section we model the observed silicate feature and the underlying continuum emission in terms of the combined thermal emission from silicate and absorbing particles. We assume a broad size distribution for the particles in the coma. By analogy with the chondritic aggregate IDPs of likely cometary origin, we assume that particles larger than a couple of microns are aggregates of smaller grains. There is sufficient dark absorbing material, such as carbon, in these aggregates to make them efficient absorbers of light. For particles with $a \lesssim 1 \mu\text{m}$, we assume that the aggregates break apart into their constituent components — silicate grains of various mineralogy and small absorbing grains.

The thermal emission from a single grain depends on its temperature and wavelength-dependent emissivity:

$$F_\lambda = \frac{4\pi a^2}{4\pi \Delta^2} \epsilon(\lambda) \pi B_\lambda(T), \quad (4)$$

where $\epsilon(\lambda)$ is the emissivity for a grain of radius a at wavelength λ and $B_\lambda(T(a))$ is the Planck function for grain temperature $T(a)$.

The temperature of small absorbing grains in the solar radiation field near 1 AU is strongly size-dependent. Absorbing particles with $a \lesssim 1 \mu\text{m}$ will be significantly hotter than a blackbody because they absorb efficiently at visual wavelengths but cannot radiate efficiently near the peak of the Planck function in the infrared. The temperature does not depend on the exact composition (Hanner 1983). Here, we use the optical constants of glassy carbon (Edoh 1983). Temperatures as a function of grain size and heliocentric distance are computed by equating the total energy absorbed to the total energy radiated, using emissivities computed by Mie theory (Hanner 1983; Hanner et al. 1999). Absorbing particles larger than a couple of microns will have temperatures close to the theoretical black body temperature (Hanner 1983).

In contrast, small silicate grains radiate efficiently in the infrared; their temperature is controlled by the amount of absorption at visual wavelengths (Hanner et al. 1999). Dorschner et al.

(1995) have shown that the imaginary index of refraction, k , at visual wavelengths depends upon the Fe/Mg ratio in the silicate. Mg-rich silicates have low absorption ($k < 0.001$) and consequently would have temperatures significantly below the blackbody temperature. The cometary silicates do appear to be Mg-rich, based on the Halley flyby dust data (Schulze et al. 1997), spectral matches (Crovisier et al. 1997), and the composition of silicates in IDPs of probable cometary origin. However, the cometary silicate grains may well be physically associated with absorbing material that raises their temperature above that of a pure silicate. Moreover, glassy silicate grains (GEMS) common in probable cometary IDPs have Fe-Ni inclusions (Bradley 1994) that serve to increase k to ~ 0.01 . Such grains will have temperatures close to the blackbody temperature near $r_h = 1$ AU.

For the present modeling, we have taken a conservative approach and adopted a temperature for the small silicate grains equal to the blackbody temperature at each heliocentric distance. One has to keep this point in mind when considering the relative abundances of various silicate minerals necessary to fit the spectra, since relative abundance will vary inversely with temperature.

The small absorbing grains and larger aggregates are represented by a smooth size distribution of the form

$$n(a) = \left[1 - \frac{a_0}{a}\right]^M \left[\frac{a_0}{a}\right]^N \quad (5)$$

where a_0 is the minimum grain radius and M is related to the peak grain size (the size where $n(a)$ is maximum), $a_p = a_0(M + N)/N$ (Hanner 1983; Hanner et al. 1985). N defines the slope of the power-law size distribution at large a ; we take $N = 3.7$ for the size distribution in the coma, corresponding to $N = 4.2$ for the dust emitted from the nucleus when the size-dependent dust velocity is taken into account. Note that for $N < 4.0$, the mass of the dust is concentrated in the largest grains, although the small grains are more numerous.

Li & Greenberg (1998) have proposed that the comet dust consists of large, extremely fluffy aggregates of submicron grains, with porosity $\sim 97\%$. Such high porosity means that the constituent submicron grains have little influence on each other; each grain tends to interact individ-

ually with the radiation field at the wavelengths considered here. Xing & Hanner (1997) showed that aggregates of absorbing grains with porosity $\leq 63\%$ (resembling the cometary IDPs) have temperatures equal to a volume equivalent sphere, while aggregates with porosity $> 80\%$ will have temperatures approaching the temperature one would compute for the constituent grains. (See also the discussion of dust models for Hale-Bopp in Brucato et al. (1999).) In our models of temperature versus dust particle size, we are implicitly assuming that the particles larger than a couple of microns have porosity $\leq 63\%$ and that the submicron dust particles are *either* individual grains or aggregates of submicron grains with porosity $\gg 80\%$. We will continue to use the term “grain” to refer to these submicron units.

The strong 3–5 μm thermal emission and high color temperature seen in our data and other Hale-Bopp data (Williams et al. 1997; Mason et al. 1999) tell us immediately that there are abundant hot submicron sized grains present. To determine the parameters a_0 and a_p in Equation 5, we fit the continuum emission for those cases where we have 3.7–4.9 μm data, since it is the 4.5-to-8 μm flux ratio that places the tightest constraints on the size distribution. Figure 18a compares the March 28.029 spectrum of the nuclear region with our best fitting model having $a_0 = 0.05 \mu\text{m}$ and $a_p = 0.13 \mu\text{m}$. Figure 18b shows the best fit for the March 28.031 spectrum at 4'' S of the nucleus, in the region just behind the jet where the color temperature feature is somewhat lower (see Figs. 7 and 13a). Here, the best fit corresponds to $a_0 = 0.05 \mu\text{m}$ and $a_p = 0.16 \mu\text{m}$. The small peak radius contrasts to other comets, where a_p is typically 0.3–0.54 μm at $r_h \lesssim 1$ AU when a similar form of $n(a)$ is assumed (Hanner et al. 1985), and confirms the qualitative conclusions about the relatively large abundance of small grains in Hale-Bopp. The minimum radius of 0.05 μm is also smaller than that used for other comets (typically 0.1 μm); we cannot fit the high 3–5 μm flux in Hale-Bopp in 1997 with $a_0 \geq 0.1 \mu\text{m}$. Grains smaller than 0.05 μm may be present but their contribution to the total thermal flux will be small, so they are “invisible” to our modeling. The silicate grains contribute $\ll 1\%$ to the 3–5 μm continuum and about 5% to the 8 μm continuum.

The distinct spectral structure in the silicate

feature is caused by the different silicate minerals present. We model this structure by using emissivities of silicate minerals measured in the laboratory (Stephens & Russell 1979; Sandford & Walker 1985). The $11.2\ \mu\text{m}$ peak and the $11.8 - 11.9\ \mu\text{m}$ shoulder are due to crystalline olivine, $(\text{Mg, Fe})_2\text{SiO}_4$, first detected in the spectrum of Comet Halley (Bregman et al. 1987; Campins & Ryan 1989). The $16-30\ \mu\text{m}$ spectra of Hale-Bopp at 2.9 AU taken from ISO show several strong peaks of Mg-rich crystalline olivine (Crovisier et al. 1997), confirming this identification. Three grain components may contribute to the broad maximum at $10\ \mu\text{m}$: the crystalline olivine responsible for the $11.2\ \mu\text{m}$ peak, glassy olivine, and crystalline pyroxene. The shoulder at $9.3\ \mu\text{m}$, seen for the first time in Comet Hale-Bopp, marks the presence of pyroxene $(\text{Mg, Fe})\text{SiO}_3$, probably amorphous enstatite (Hanner et al. 1999; Wooden et al. 1999; Stephens & Russell 1979).

Crystalline pyroxenes have considerable variety in their spectral shape (Sandford & Walker 1985; Koike 1993; Wooden et al. 1999); they may contribute to the spectral structure at 9.3 , 10.0 , and $10.5\ \mu\text{m}$. In our models, we have used the spectra of “Key” and “Spray 1” pyroxene-rich IDPs from Sandford & Walker (1985) in addition to the emissivity of orthorhombic enstatite from Stephens & Russell (1979).

The relative contributions of the various silicate components were varied until a good match to the observed spectral shape was obtained. The relative contributions of the components and the resulting silicate emissivity template we used are shown in Figure 19. If the components have similar sizes and temperatures, then amorphous pyroxene is the most abundant silicate ($\gtrsim 40\%$) and the pyroxenes together constitute about two-thirds of the total. Since the samples measured in the laboratory undoubtedly do not match the cometary silicate particles exactly in size, shape, or composition, a more detailed specification of the relative abundances is not warranted.

The final model, then, consists of thermal emission from the size distribution of absorbing particles, plus thermal emission from silicate grains based on the emissivity template in Figure 19 and assuming a temperature for the silicate grains equal to the blackbody temperature. Figure 18 shows our best fit to the $3-13\ \mu\text{m}$ March 28.031

spectra.

Model fits to four additional $8-13\ \mu\text{m}$ spectra are displayed in Figure 20. The spectra represent different dates (February, March) and positions (the nuclear region vs. the jet). The same silicate template matches the shape of all four spectra; the fit is within 5% at all wavelengths. The only free parameters adjusted in the fits are a small shift in a_p , affecting the color temperature of the continuum, and the ratio of silicate to absorbing grains (stronger silicate feature within jets). These fits are consistent with the results discussed in § 3; the silicate feature/continuum ratio and the color temperature of the underlying continuum vary with position in the coma, but the shape of the silicate feature appears to remain constant.

Our approach, in which separate grain components account for the silicate feature and the underlying continuum emission, contrasts with Wooden et al. (1999), who assume that the silicate grains are hot enough to produce the continuum, with the exception of the crystalline pyroxenes, which are assumed to be clean and cold, in order to explain changes in spectral shape with heliocentric distance. Such a wide difference in temperature among the silicate components requires that the hot silicates are either very iron-rich, or preferentially associated with carbonaceous material, while the crystalline pyroxene grains are Mg-rich and free of absorbing material. We do not see evidence that the pyroxene in comets is more Mg-rich than the crystalline olivine (e.g., Crovisier et al. 1997), nor any reason why one component should have less contact with absorbing material, unless there is a systematic difference in the grain size among the components. Wooden et al. (1999) attribute the $9.3\ \mu\text{m}$ peak to crystalline pyroxenes while we attribute it to amorphous pyroxenes. The large temperature difference in the Wooden et al. model leads to a very high abundance of crystalline pyroxene relative to the other components, whereas in our models the amorphous pyroxene is the most abundant component.

5. Discussion

5.1. Comparison with Polarization Observations

We have been discussing the relation between the color temperature, the silicate feature

strength, and the size of the grains. Another optical property that is sensitive to dust grain size and composition is the polarization. The linear polarization in comet Hale-Bopp at phase angles $> 22^\circ$ was consistently higher than that measured for any other comet at the same phase angles (e.g., Jockers 1999; Jones & Gehrz 1999). In addition, polarization images of the inner coma obtained by Jockers et al. (1999), Jones & Gehrz (1999), Hadamcik et al. (1999), and Furusho et al. (1999) clearly show that the polarization is enhanced in the jets and halos.

Previous researchers have noted that higher polarization in comets correlates with a stronger silicate feature (e.g., Levasseur-Regourd, Hadamcik, & Renard 1996). For grain radii a few tenths of a micron or larger, silicate grains tend to have relatively low positive polarization and more negative polarization, while carbonaceous grains show stronger positive polarization (Yanamandra-Fisher & Hanner 1999); this is not consistent with the association of higher polarization with stronger silicate feature. Only for grain radii $\sim 0.1 \mu\text{m}$ and smaller does the maximum polarization near 90° increase for both silicate and absorbing grains.

Thus, there are several indicators that comet Hale-Bopp near perihelion was richer in small (submicron) particles than the dust in other well-observed comets. These include the higher ratio of color temperature to blackbody temperature (“superheat”), the strong 3–5 μm flux, the strength of the silicate feature above the continuum (2–3 for Hale-Bopp, $\lesssim 2$ for other comets), strength of the scattered light continuum, higher albedo, and higher polarization at comparable phase angles, particularly within the jets.

5.2. Comparison of the Silicate Feature with Other Comets

How does the silicate spectrum in Hale-Bopp compare with other comets? In retrospect, comets 1P/Halley, Levy (C/1990 K1), Bradfield (C/1987 P1), and Mueller (C/1993 A1) all show similar silicate spectral features, with the 9.3 μm shoulder, broad 10 μm maximum, and 11.2 μm peak. The 9.3 μm shoulder was not identified previously because of the interference from the 9.5 μm telluric feature in these weaker spectra. However, the possibility of pyroxene was recognized (e.g., Sandford

& Walker 1985; Bregman et al. 1987; Hanner et al. 1994a).

To investigate the similarity in silicate composition among these comets, we have applied the models developed in § 4.2 to fit the thermal emission spectra of the above-mentioned comets. The *same* mix of silicate minerals as shown in Figure 19 is retained. The grain temperatures are computed for the appropriate heliocentric distances. The only adjustable parameters are the peak size, a_p in Equation 5, which affects the color temperature in the continuum spectral energy distribution, and the ratio of the silicate feature strength to the continuum at 10 μm .

The model fit to comet Mueller at 2 AU, along with a comparison of the flux/continuum profile to that of Hale-Bopp, is presented in Figure 21. One sees that the model closely matches the spectral shape of the silicate feature in this new Oort Cloud comet, indicating that the silicate dust in comet Mueller is very similar to that in Hale-Bopp.

Figure 22 compares the model to the 5–13 μm spectrum of comet Halley (Bregman et al. 1987). While the 5–13 μm continuum, the 11.2 μm peak, and the overall shape of the silicate feature fit well, the 10 μm peak is broader and flatter in comet Halley than in Hale-Bopp near perihelion. Spectra of Halley at 0.79 AU, Levy at 1.54 AU, Bradfield at 0.99 and 1.45 AU, and Kohoutek at 0.31 AU all show a broader, flatter 10 μm maximum than that displayed by Hale-Bopp in 1997 February – April (Hanner et al. 1994b).

Although the flatter 10 μm peak could mean that the silicate composition differs somewhat among comets, it could also result from a difference in the dust size distribution. Figure 3 in Hanner et al. (1987), for example, shows how the 10 μm peak in glassy olivine broadens and flattens as the grain radius increases to 1 μm and larger. Variations in temperature among the silicates could also cause differences in the spectral shape as described by Wooden et al. (1999), but the differences in spectral shape with heliocentric distance are not consistent among the comets, as one would expect if temperature variations were responsible. While the 10 μm peak is sharper in Hale-Bopp near perihelion, it is flatter in Halley at 0.79 AU and in Kohoutek at 0.31 AU, yet prominent in Mueller at 2 AU.

5.3. Implications of the Silicate Spectra

One of the major advances from IR spectroscopy of comet Hale-Bopp, both our data and those of others (Russell et al. 1997; Wooden et al. 1999; Hanner et al. 1999), is the identification of the silicate mineralogy. The spectral structure in the $10\ \mu\text{m}$ emission feature clearly bears the signature of both crystalline and non-crystalline silicates of both olivine and pyroxene composition. Such a mineral mixture is typical of the anhydrous chondritic aggregate interplanetary dust particles (IDPs) swept up by the Earth and retrieved from the stratosphere for laboratory analysis. This type of IDP has been identified previously as cometary because of the aggregate structure of small ($0.1 - 1\ \mu\text{m}$) grains, high carbon content, silicates with high Mg/Fe abundance, and relatively high atmospheric entry velocities; the Hale-Bopp spectra strengthen this identification.

The spectra of chondritic IDPs divide into three classes, dominated by olivine, pyroxene, and layer lattice silicates respectively (Sandford & Walker 1985). The hydrated silicate IDPs are more compact, have lower atmospheric entry velocities, and are mineralogically similar to the fine-grained matrix material in carbonaceous chondrites; these IDPs are probably asteroidal in origin (Sandford & Bradley 1989). While the spectra of the anhydrous IDP classes tend to be dominated by relatively large crystals of olivine and pyroxene, the most abundant silicates by number are the small ($0.1-0.5\ \mu\text{m}$) GEMS – glass with embedded metal and sulfides (Bradley 1994). The infrared spectra of individual GEMS show a broad, smooth spectral feature peaking at either 9.3 or $9.7 - 10.1\ \mu\text{m}$, consistent with the features in the comet spectra (Bradley et al. 1999). Spectra of two glass-rich porous IDPs studied by Bradley et al. (1992) have broad, multi-peaked spectra that are similar to the Hale-Bopp spectra.

The mix of high temperature (crystalline) and low temperature (glassy or amorphous) condensates in the cometary dust suggests a complex history for the silicate material prior to incorporation into the comet nucleus. Bradley (1994) and Bradley et al. (1999) have presented convincing arguments that the GEMS are of interstellar origin. The $10\ \mu\text{m}$ spectra of GEMS indeed resemble the broad structureless silicate spectrum of the ISM.

These grains would have been present in the cold outer solar nebula where the comet nuclei formed.

The crystalline silicates are more puzzling (see discussion in Hanner et al. (1994a) and Hanner et al. (1999)). Crystalline grains can form by direct condensation from the vapor phase at $1200 - 1400\ \text{K}$. Direct condensation provides a natural explanation for the Mg-rich silicates, since forsterite and enstatite are the first to condense in a hot gas and only react with iron at a lower temperature. While their spectral signature is evident in the cooling outflows of AGB stars, spectral evidence for crystalline silicates is missing in the ISM. Since silicates can be rather efficiently destroyed in interstellar shocks, perhaps the only AGB silicates that survived had thick organic refractory mantles (e.g., Greenberg & Hage 1990) which masked their spectral features. Alternatively, the crystalline particles could have formed by direct condensation or annealing in the inner solar nebula. Disk midplane temperatures $> 1000\ \text{K}$ were reached at $r_h \lesssim 1\ \text{AU}$ (Chick & Cassen 1997). But this would require considerably more radial mixing of particulates in the solar nebula than present models predict; the problem is that growth by accretion was relatively rapid, limiting the radial diffusion (Cuzzi et al. 1993). The spectra of young stellar objects do not show crystalline silicates, except for stars with debris disks such as β Pictoris (Knacke 1993), or late-stage Herbig Ae/Be stars (Malfait et al. 1998; Sitko et al. 1999). In each of these cases, the dust is attributed to a population of star-grazing comets which give rise to transient gaseous emission features (e.g., Grady et al. 1997).

6. Conclusions

In this paper, we have described a $\lambda = 3-13\ \mu\text{m}$ imaging and spectroscopic study of the dust component of comet Hale-Bopp. Our principal results are as follows:

1. As in many comets, the infrared SED of Hale-Bopp was composed of continuum and silicate feature components. The $10\ \mu\text{m}$ silicate feature was already observed to be very strong at the large heliocentric distance $r_h = 4.2\ \text{AU}$. Near perihelion the ratio of the $3-5\ \mu\text{m}$ continuum color temperature to the blackbody equilibrium temperature (the superheat) was ~ 1.8 , and the

flux-to-continuum ratio of the $10\ \mu\text{m}$ feature was as high as 3.3, higher than observed for any previous comet. These observations demonstrate that submicron dust grains were a significant component of Hale-Bopp. A grain emission model fitted to the SED near perihelion indicates that a size distribution of absorbing grains peaking at $a \approx 0.13\ \mu\text{m}$ gives a good match, compared to $a \approx 0.3\text{--}0.54\ \mu\text{m}$ typical of other comets at $r_h < 1\ \text{AU}$. The strong silicate feature also indicates an unusually high abundance of submicron silicate grains relative to the absorbing grains.

2. Within $\sim 1''$ of the nucleus, the $8\text{--}13\ \mu\text{m}$ superheat varied only slightly, from about 1.3 to 1.4 as the comet traveled from $r_h = 4.2$ to $0.92\ \text{AU}$, but the silicate feature flux-to-continuum ratio increased from 1.8 to 3.0 during this time and was as high as 3.3 a few weeks after perihelion. These variations may indicate a gradual change in the ratio of silicate to absorbing grains or a disaggregation of larger particles as the comet approached the sun.
3. Our image cubes and long-slit spectra allow us to examine the spatial variation of dust emission properties in the inner coma, including the prominent jets and halos. We find that the continuum color temperature and silicate feature strength are both elevated in the jets and halos relative to neighboring regions in the coma, probably due to sorting effects caused by the different ejection velocities of small and large particles. We do not see evidence for radial variations, either in the halos or outside the halos, that would indicate a time-dependent fragmentation of grains as they flowed outward from the nucleus.
4. We have presented preliminary modeling of dust particle motions for several sizes of absorbing particles and silicate grains, corresponding to discrete range in β . There is a good correspondence between the models and the morphology displayed in our infrared mosaics and image cubes. The regions of highest T_c and silicate feature strength

correspond to the loci of the smaller particles. The synthetic images suggest that only grains with $\beta < 1$ can explain the uniform spacing of the halos in our infrared mosaics in February and March 1997. For these grains, v_{eject} dominates their motion on the time scale of one or two nuclear rotations.

5. The $8\text{--}13\ \mu\text{m}$ silicate feature displayed prominent peaks at 11.2 and $10.0\ \mu\text{m}$, attributed to crystalline and amorphous olivine, respectively, as well as a distinct shoulder at $9.3\ \mu\text{m}$, in agreement with other high-quality Hale-Bopp spectra (Wooden et al. 1999). The $9.3\ \mu\text{m}$ feature, newly discovered in Hale-Bopp, is a signature of pyroxene composition. The discovery of pyroxene in Hale-Bopp further strengthens the connection between cometary dust and IDPs collected in the stratosphere, which are known from laboratory analysis to contain both pyroxene and olivine.
6. Although the $10\ \mu\text{m}$ silicate feature varied in overall strength, the spectral structure of the feature remained nearly constant in at least a two month timespan around perihelion passage. We also observed no change in spectral shape between the nuclear region, jets, halos, and diffuse part of the coma. Our spectral model with a single mixture of amorphous and crystalline olivines and pyroxenes fits the various spectra equally well. This indicates a uniform mineralogical composition of the nucleus. However, before 1996 September ($r_h > 3\ \text{AU}$), the main $10\ \mu\text{m}$ peak was broader.
7. The overall shape of the silicate feature resembled that in other bright comets, indicating a similar mineral mix. However, the $10.0\ \mu\text{m}$ peak was sharper in Hale-Bopp in 1997 than in any previously observed comet with the exception of comet Mueller (C/1993 A1) at $2\ \text{AU}$.

Our extensive set of spatially resolved thermal-IR images and spectra provide new constraints on the dynamical modeling of coma morphology. We are currently modifying the Monte Carlo simulation code to calculate explicitly the thermal emission at each position, as a function of grain size

and composition. In parallel, the thermal modeling will evaluate the effects of grain mantles, aggregate structure, and porosity on the color temperature and strength of the silicate feature.

We thank the staff of Palomar Observatory for assistance with the observations, many of which were conducted under challenging conditions. T. Hayward's research was supported by NASA grant NAGW-2551 and the Department of Astronomy at Cornell University. M. Hanner's and Z. Sekanina's research was carried out at the Jet Propulsion Laboratory, California Institute of Technology, under contract with the National Aeronautics and Space Administration.

REFERENCES

- Bradley, J. P. 1994, *Science*, 265, 925
- Bradley, J. P., Humecki, H. J., & Germani, M. S. 1992, *ApJ*, 394, 643
- Bradley, J. P., Keller, L. P., Snow, T. P., Hanner, M. S., Flynn, G. J., Gezo, J. C., Clemett, S. J., Brownlee, D. E., & Bowey, J. E. 1999, *Science*, 285, 1716
- Bregman, J. D., Campins, H., Witteborn, F. C., Wooden, D. H., Rank, D. M., Allamandola, L. J., Cohen, M., & Tielens, A.G.G.M. 1987, *A&A*, 187, 616
- Brucato, J. R., Colangeli, L., Mennella, V., Palumbo, P. & Bussoletti, E. 1999, *Plan. Space Sci.*, 47, 773
- Burns, J. A., Lamy, P. L., & Soter, S. 1979, *Icarus*, 40, 1
- Campins, H., & Ryan, E. 1989, *ApJ*, 341, 1059
- Chick, K. M., & Cassen, P. 1997, *ApJ*, 477, 398
- Cohen, M., Walker, R. G., Barlow, M. J., & Deacon, J. R. 1992, *AJ*, 104, 1650
- Crovisier, J. et al. 1996, *A&A*, 315, L385
- Crovisier, J., Leech, K., Bockl e-Morvan, D., Brooke, T. Y., Hanner, M. S., Altieri, B., Keller, H. U., & Lellouch, E. 1997, *Science*, 275, 1904
- Cuzzi, J. N., Dobrovolskis, A. R., & Champney, J. M. 1993, *Icarus*, 106, 102
- Dorschner, J., Begemann, B., Henning, Th. Jager, C., & Mutschke, H. 1995, *A&A*, 300, 503
- Edoh, O. 1983, Ph.D. dissertation, Dept. of Physics, Univ. Arizona
- Fern andez, Y. R. et al. 1999, *Icarus*, 140, 205
- Fern andez, Y. R., Lisse, C. M., & A'Hearn, M. F. 1999, *Earth, Moon, & Planets*, in press
- Furusho, R., Suzuki, B., Yamamoto, N., Kawakita, H., Sasaki, T., Shimizu, Y., & Kurakami, T. 1999, *PASJ*, 51, 367
- Galdemard, P., Lagage, P. O., Pantin, E., Dubreuil, D., Jouan, R., Masse, P., & Bockl e-Morvan, D. 1999, *Earth, Moon, & Planets*, in press
- Gehrz, R. D., & Ney, E. P. 1992, *Icarus*, 100, 162
- Gehrz, R. D., Johnson, C. H., Magnuson, S. D., Ney, E. P., & Hayward, T. L. 1995, *Icarus*, 113, 129
- Grady, C. A., Sitko, M. L., Bjorkman, K. S., Perez, M. R., Lynch, D. K., Russell, R. W., & Hanner, M. S. 1997, *ApJ*, 483, 449
- Greenberg, J. M., & Hage, J. I. 1990, *ApJ*, 361, 260
- Hadamcik, E., Levasseur-Regourd, A. C., & Renard, J. B. 1999, *Earth, Moon, & Planets*, in press
- Hanner, M. S. 1983, in *Cometary Exploration*, ed. T.I. Gombosi, *Hungar. Acad. Sciences*, II, p. 1
- Hanner, M. S., et al. 1999, *Earth, Moon, & Planets*, in press
- Hanner, M. S., Hackwell, J. A., Russell, R. W., & Lynch, D. K. 1994a, *Icarus*, 112, 490
- Hanner, M. S., Lynch, D. K., & Russell, R. W. 1994b, *ApJ*, 425, 274
- Hanner, M. S., Tedesco, E., Tokunaga, A. T., Veeder, G. J., Lester, D. F., Witteborn, F. C., Bregman, J. D., Gradie, J., & Lebofsky, L. 1985, *Icarus*, 64, 11
- Hanner, M. S., Tokunaga, A. T., Golisch, W. F., Griep, D. M., & Kaminski, C. D. 1987, *A&A*, 187, 653
- Hayward, T. L., & Hanner, M. S. 1997, *Science*, 275, 1903
- Hayward, T. L., & Hanner, M. S. 1999, *Earth, Moon, & Planets*, in press
- Hayward, T. L., Miles, J. W., Houck, J. R., Gull, G. E., & Schoenwald, J. 1993, *Proc. SPIE*, 1946, 334

- Jockers, K. 1999, *Earth, Moon, and Planets*, in press
- Jockers, K., Rosenbush, V. K., Bonev, T., & Credner, T. 1999, *Earth, Moon, and Planets*, in press
- Jones, T. J., & Gehrz, R. D. 1999, *Icarus*, in press
- Jorda, L., Lecacheux, J., & Colas, F. 1997, *IAU Circ.* 6583
- Koike, C., Shibai, H., & Tuchiya, A. 1993, *MNRAS*, 264, 654
- Knacke, R. F., Fajardo-Acosta, S. B., Telesco, C. M., Hackwell, J. A., Lynch, D. K., & Russell, R. W. 1993, *ApJ*, 418, 440
- Levasseur-Regourd, A. C., Hadamcik, E., & Renard, J. B. 1996, *A&A*, 313, 327
- Li, A., & Greenberg, M. 1998, *ApJ*, 498, L83
- Licandro, J., et al. 1998, *ApJ*, 501, L221
- Lisse, C. M., et al. 1999, *Icarus*, 140, 189
- Lord, S. 1992, *A New Software Tool for Computing Earth's Atmospheric Radiation*, NASA Tech. Mem. 103957
- Malfait, K., Waelkens, C., Waters, L. B. F. M., Vandenbussche, B., Huygen, E., & de Graauw, M. S. 1998, *A&A*, 332, L25
- Mason, C. G., Gehrz, R. D., Jones, T. J., Hanner, M. S., Williams, D. M., & Woodward, C. E. 1999, *BAAS*, 194, 1502
- Russell, R. W., Lynch, D. K., Mazuk, A. L., Rossano, G. S., Hanner, M. S. & Sitko, M. L. 1997, *BAAS*, 29, 1041
- Sandford, S. A., & Bradley, J. P. 1989, *Icarus*, 82, 146
- Sandford, S. A., & Walker, R. M. 1985, *ApJ*, 291, 838
- Sarmecanic, J., Osip, D. J., Fomenkova, M., & Jones, B. 1997, *IAU Circ.* 6600
- Schleicher, D. G., Farnham, T. L., Smith, B. R., Nielsen, E., & Lederer, S. M. 1998, *BAAS*, 30, 2907
- Schulze, H., Kissel, J., & Jessberger, E. K. 1997, in *From Stardust to Planetesimals*, ed. Y. Pendleton & A.G.G.M. Tielens, ASP Conf. Series 122, 397
- Sekanina, Z. 1981, *AJ*, 86, 1741
- Sekanina, Z. 1991, *AJ*, 494, L121
- Sekanina, Z. 1996, in *Physics, Chemistry, and Dynamics of Interplanetary Dust*, ed. B.A.S. Gustafson & M.S. Hanner, ASP Conf. Series 104, 377
- Sekanina, Z. 1998a, *ApJ*, 494, L121
- Sekanina, Z. 1999, *Earth, Moon, & Planets*, in press
- Sekanina, Z., & Larson, S. M. 1984, *AJ*, 89, 1408
- Sekanina, Z., & Larson, S. M. 1986, *AJ*, 92, 462
- Sitko, M. L., Grady, C. A., Lynch, D. K., Russell, R. W., & Hanner, M. S. 1999, *ApJ*, 510, 408
- Stephens, J. R., & Russell, R. W. 1979, *ApJ*, 228, 780
- Tokunaga, A. T. 1984, *AJ* 89, 172
- Vasundhara, R., & Chakraborty, P. 1999, *Icarus*, 140, 221
- Weaver, H. A., & Lamy, P. 1999, *Earth, Moon, & Planets*, in press
- Williams, D. M., et al. 1997, *ApJ*, 489, L91
- Wooden, D. H., Harker, D. E., Woodward, C. E., Butner, H. M., Koike, C., Witteborn, F. C., & McMurtrey, C. W. 1999, *ApJ*, 517, 1034
- Xing, Z., & Hanner, M. S. 1997, *A&A*, 324, 805
- Yanamandra-Fisher, P. A., & Hanner, M.S. 1999, *Icarus*, 138, 107

This 2-column preprint was prepared with the AAS L^AT_EX macros v5.0.

TABLE 1
OBSERVING LOG

Date	Start UTC	End UTC	Airmass	Standard Star ^a	r_h (AU)	Δ (AU)	S-O-E ^b ($^\circ$)	PA ^c ($^\circ$)	T_{BB} (K)	Scale (km arcsec ⁻¹)
97 Feb 17	12:16	13:59	4.9–1.8	6, 7	1.18	1.68	35.1	325.3	257	1218
19	12:16	14:04	4.7–1.8	6, 7	1.16	1.65	36.3	325.5	259	1196
Mar 24-25	22:23	2:38	1.1–2.8	1, 2	0.92	1.32	49.1	8.2	291	957
25-26	22:51	2:12	1.2–2.4	3, 4	0.92	1.32	49.0	10.6	291	957
26-27	22:48	2:09	1.1–2.1	3	0.92	1.32	48.9	13.0	291	957
27-28	23:00	2:20	1.2–2.2	3	0.92	1.33	48.7	15.7	291	964
Apr 19	2:24	3:35	1.8–2.6	4, 5	0.97	1.57	38.0	58.9	283	1139

^a1 = β And, 2 = α Aur, 3 = α Tau, 4 = α CMa, 5 = β Gem, 6 = α Lyr, 7 = γ Aql.

^bSun–Object–Earth angle.

^cDirection from Sun to Object on sky, degrees east of north.

TABLE 2
IMAGES^a

No.	1997 Date	Start UTC	End UTC	Airmass	n^b	λ (μm)	N_{rot}^c	Notes
1	Feb 17.515	12:16	12:27	4.96-4.25	7	7.9-17.9	0.693	poor nodding
2	Feb 17.539	12:39	13:14	3.63-2.58	1	10.3	0.745	mosaic
3	Feb 17.556	13:17	13:25	2.52-2.38	7	7.9-17.9	0.781	some clouds
4	Feb 17.584	13:57	14:05	1.91-1.83	7	"	0.840	
5	Feb 19.516	12:16	12:31	4.66-3.85	7	7.9-17.9	4.950	poor seeing
6	Feb 19.530	12:33	12:52	3.71-3.04	7	7.9-17.9	4.978	mosaic
7	Feb 19.542	12:55	13:05	2.96-2.72	7	7.9-17.9	5.003	
8	Feb 19.585	14:01	14:05	1.83-1.81	7	7.9-17.9	5.096	
9	Mar 24.935	22:23	22:29	1.13-1.13	7	7.9-17.9	1.482	seeing poor
10	Mar 24.959	22:59	23:04	1.20-1.21	6	7.9-12.5	1.535	"
11	Mar 24.982	23:27	23:42	1.30-1.32	6	"	1.583	"
12	Mar 25.041	00:56	01:01	1.68-1.71	6	"	1.707	seeing improving
13	Mar 25.053	01:14	01:19	1.81-1.85	6	"	1.733	"
14	Mar 25.064	01:29	01:34	1.94-1.98	6	"	1.755	good seeing
15	Mar 25.078	01:50	01:55	2.16-2.21	6	"	1.786	"
16	Mar 25.091	02:09	02:14	2.40-2.47	6	"	1.814	"
17	Mar 25.099	02:16	02:30	2.51-2.74	1	11.7	1.831	mosaic
18	Mar 25.106	02:31	02:34	2.78-2.84	6	7.9-12.5	1.845	some pixels saturating
19	Mar 25.956	22:51	23:01	1.17-1.18	8	4.2-17.9	3.642	seeing poor
20	Mar 25.984	23:35	23:40	1.28-1.29	6	7.9-12.5	3.703	"
21	Mar 25.990	23:41	23:50	1.30-1.32	8	4.2-17.9	3.715	"
22	Mar 26.056	01:16	01:26	1.78-1.85	8	"	3.856	seeing better
23	Mar 26.069	01:35	01:43	1.94-2.02	1	11.7	3.882	small mosaic in tail
24	Mar 26.076	01:46	01:52	2.04-2.11	8	4.2-17.9	3.897	seeing good
25	Mar 26.089	02:05	02:12	2.27-2.37	8	"	3.925	"
26	Mar 26.953	22:49	22:55	1.15-1.16	8	4.2-17.9	5.749	cirrus clouds
27	Mar 26.969	23:12	23:18	1.20-1.21	8	"	5.783	"
28	Mar 26.981	23:30	23:36	1.24-1.26	8	"	5.810	"
29	Mar 26.993	23:47	23:53	1.29-1.31	8	"	5.834	"
30	Mar 27.004	00:03	00:09	1.35-1.37	8	"	5.858	"
31	Mar 27.016	00:20	00:27	1.42-1.45	8	"	5.884	"
32	Mar 27.032	00:43	00:50	1.53-1.56	8	"	5.917	"
33	Mar 27.046	01:03	01:09	1.64-1.68	8	"	5.946	"
34	Mar 27.058	01:11	01:36	1.70-1.89	1	11.7	5.972	mosaic, cirrus
35	Mar 27.070	01:38	01:45	1.91-1.96	8	4.2-17.9	5.998	cirrus clouds
36	Mar 27.075	01:45	01:52	1.98-2.04	8	"	6.008	"
37	Mar 27.081	01:53	02:00	2.06-2.12	8	"	6.020	"
38	Mar 27.961	23:01	23:08	1.16-1.17	8	4.2-17.9	7.879	good seeing
39	Mar 27.985	23:28	23:49	1.22-1.28	1	10.3	7.928	mosaic
40	Mar 28.001	23:50	00:11	1.29-1.36	1	7.9	7.961	"
41	Mar 28.015	00:11	00:33	1.36-1.45	1	12.5	7.992	"
42	Mar 28.037	00:50	00:57	1.53-1.57	8	4.2-17.9	8.038	
43	Mar 28.091	02:08	02:15	2.16-2.23	8	"	8.153	
44	Apr 19.102	02:24	02:30	1.77-1.82	8	4.2-17.9	1.684	fair seeing
45	Apr 19.118	02:49	02:51	2.02-2.04	1	11.7	1.718	mosaic, aborted
46	Apr 19.129	02:51	03:20	2.04-2.47	1	10.3	1.742	mosaic
47	Apr 19.142	03:21	03:27	2.51-2.60	8	4.2-17.9	1.769	11.7 & 12.5 saturating

^aEach entry represents several individual integrations that compose a multi-wavelength image cube or a single-wavelength mosaic.

^b n = number of filter settings in the image sequence.

^c N_{rot} = number of nuclear rotations since t_0 , defined to be February 17.189, March 24.235, and April 18.310 for the February, March, and April data, respectively, which correspond to "midnight" times at Source A on the nucleus.

TABLE 3
SPECTRA^a

No.	1997 Date	Start UTC	End UTC	Airmass	n^b	λ (μm)	Slit	N_{rot}^c	Notes
1	Feb 17.563	13:28	13:34	2.30-2.23	3	8-13	2''	0.796	nucleus, poor
2	Feb 17.570	13:38	13:45	2.14-2.08	3	"	1''	0.811	nucleus
3	Feb 17.577	13:47	13:54	2.02-1.96	3	"	"	0.825	7'' S
4	Feb 19.559	13:10	13:41	2.58-2.08	3	8-13	1''	5.041	3 segs 5'' N to 30'' S
5	Feb 19.577	13:42	14:01	2.06-1.86	3	"	"	5.008	10'' W, 5'' N to 30'' S
6	Mar 24.947	22:32	22:56	1.14-1.19	3	8-13	1''	1.509	4 segs 5'' N to 30'' S
7	Mar 24.965	23:05	23:14	1.21-1.23	3	"	"	1.546	10'' N
8	Mar 24.974	23:19	23:25	1.24-1.26	3	"	"	1.565	60'' S
9	Mar 24.980	23:28	23:34	1.27-1.29	3	"	"	1.578	30'' E, 30'' S
10	Mar 24.990	23:43	23:48	1.32-1.33	3	"	"	1.599	nucleus
11	Mar 25.045	01:02	01:08	1.72-1.75	3	"	"	1.716	nucleus
12	Mar 25.050	01:09	01:14	1.77-1.80	3	"	"	1.726	2'' W
13	Mar 25.059	01:22	01:27	1.88-1.91	3	"	"	1.745	3'' W
14	Mar 25.069	01:37	01:42	2.02-2.05	3	"	"	1.767	nucleus
15	Mar 25.074	01:44	01:49	2.09-2.13	3	"	"	1.777	1'' W
16	Mar 25.083	01:56	02:02	2.24-2.28	3	"	"	1.796	2-3'' W
17	Mar 25.966	23:03	23:18	1.19-1.22	3	8-13	1&2''	3.664	nucleus
18	Mar 25.977	23:21	23:34	1.24-1.27	3	3-11	"	3.689	nucleus
19	Mar 26.064	01:29	01:34	1.89-1.91	3	8-11	"	3.871	nucleus
20	Mar 26.083	01:56	02:04	2.16-2.23	4	3-13	"	3.913	nucleus
21	Mar 26.961	22:59	22:09	1.17-1.19	5	3-13	1''	5.748	cirrus clouds, nucleus
22	Mar 26.975	23:20	23:29	1.22-1.24	5	"	"	5.777	nucleus
23	Mar 26.987	23:39	23:44	1.27-1.28	3	8-13	"	5.802	30'' S
24	Mar 26.999	23:55	00:03	1.32-1.34	5	3-13	"	5.827	nucleus
25	Mar 27.011	00:11	00:20	1.38-1.41	3	8-13	"	5.850	60'' S, clouds worse
26	Mar 27.016	00:20	00:27	1.42-1.45	3	"	"	5.862	nucleus
27	Mar 27.027	00:34	00:44	1.48-1.52	5	3-13	"	5.884	nucleus
28	Mar 27.040	00:53	01:01	1.58-1.62	5	"	"	5.910	nucleus
29	Mar 27.970	23:10	23:23	1.17-1.20	5	3-13	2''	7.896	nucleus
30	Mar 28.031	00:40	00:48	1.48-1.51	5	"	"	8.024	nucleus
31	Mar 28.046	01:02	01:11	1.59-1.65	5	"	"	8.057	15'' S
32	Mar 28.053	01:12	01:20	1.67-1.71	4	8-13	"	8.071	30'' S
33	Mar 28.060	01:22	01:30	1.74-1.78	4	"	"	8.086	45'' S
34	Mar 28.068	01:34	01:42	1.83-1.88	5	3-13	"	8.103	24'' W, 14'' S, halo
35	Mar 28.080	01:51	01:58	1.98-2.03	3	8-13	"	8.128	40'' W, 60'' N, tail
36	Mar 28.085	02:00	02:04	2.07-2.10	3	"	"	8.139	20'' W, 30'' N, tail
37	Mar 28.097	02:17	02:22	2.27-2.31	3	"	"	8.164	5'' W, jet
38	Apr 19.111	02:36	02:44	1.88-1.97	3	8-13	1''	1.704	nucleus

^aEach entry represents several individual integrations that compose a complete 2-d spectral image.

^b n = number of segments in the spectral sequence.

^c N_{rot} = Number of nuclear rotations since the time of zero rotational phase angle, defined as in Table 2.

TABLE 4
STANDARD STAR MAGNITUDES^a

Star	Sp. Type	Filters					
		7.8	8.7	9.8	10.3	11.7	12.5
α Aur	G5 III	-1.94	-1.94	-1.94	-1.94	-1.94	-1.93
β Gem	K0 III	-1.22	-1.23	-1.24	-1.25	-1.26	-1.27
α Boo	K2 III	-3.13	-3.14	-3.18	-3.19	-3.20	-3.20
γ Aql	K3 II	-0.76	-0.73	-0.80	-0.82	-0.84	-0.84
α Tau	K5 III	-3.00	-2.97	-3.06	-3.08	-3.12	-3.12
β And	M0 III	-2.01	-1.98	-2.07	-2.10	-2.15	-2.16
β Peg ^b	M2 II	-2.45	-2.44	-2.50	-2.53	-2.55	-2.55

^aMagnitudes from UKIRT CGS-3 spectra integrated over the OCLI silicate filter band profiles. Values are also consistent with IRTF photometry and are tied to the photometric system from Tokunaga (1984). Uncertainties are ± 0.05 mag for 7.8 μ m and ± 0.02 mag for all other filters.

^b β Peg is an irregular variable. Magnitudes given for mid-range; variation is $\pm 5\%$ from these values.

TABLE 5
SOURCE A EVENT TIMES AND THEIR N_{rot} QUANTITIES

	Midnight			Sunrise ^a			Sunset	
	1997 (UTC)	N_{rot}		1997 (UTC)	N_{rot}		1997 (UTC)	N_{rot}
Feb	17.189	0	Feb	17.26	0.15	Feb	17.59	0.85
	19.070	4		19.14	4.14		19.47	4.86
	19.540	5		19.61	5.14		19.95	5.86
Mar	24.235	0	
	24.707	1	
	25.652	3	
	26.598	5	
	27.071	6	
	27.545	7	
	28.019	8	
	28.019	8	
Apr	18.310	0	

^aThe sun was circumpolar at Source A during the March and April observations.

TABLE 6
SOURCE B EVENT TIMES AND THEIR N_{rot} QUANTITIES

	Midnight			Sunrise			Sunset	
	1997 (UTC)	N_{rot}		1997 (UTC)	N_{rot}		1997 (UTC)	N_{rot}
Mar	24.54	0.65	Mar	24.64	0.85	Mar	24.92	1.45
	25.01	1.65		25.11	1.85		25.39	2.45
	25.49	2.65		25.58	2.84		25.87	3.46
	25.96	3.65		26.05	3.84		26.34	4.46
	26.43	4.65		26.52	4.84		26.82	5.46
	26.91	5.65		26.99	5.84		27.29	6.47
	27.38	6.65		27.47	6.84		27.77	7.47
	27.85	7.65		27.94	7.83		28.24	8.47
Apr	18.62	0.65	Apr	18.72	0.88	Apr	18.98	1.42
	19.09	1.65		19.19	1.88		19.45	2.42

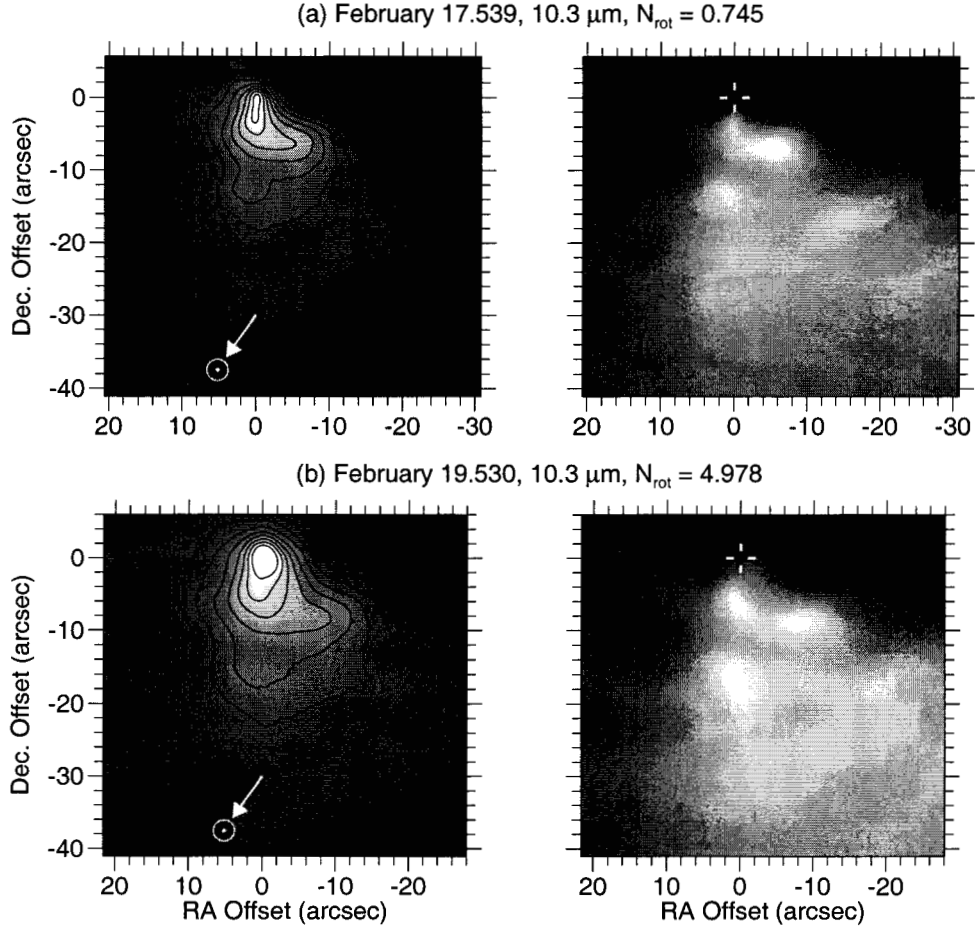


Fig. 1.— Mid-IR mosaics of comet Hale-Bopp taken in 1997 February. (Left column) Original images with isophotes. The peak isophote in each panel represents $70 \text{ Jy arcsec}^{-2}$, and the ratio between isophotes is $\sqrt{2}$. The direction to the sun in the plane of the sky is indicated by the arrow. The spatial scale is about $1200 \text{ km arcsec}^{-1}$ on both dates (see Table 1). (Right column) Images after dividing by a circularly symmetric, $1/\rho$ gradient image smoothed with the instrumental PSF, which enhances the jet and halos. N_{rot} is the number of nuclear rotations since sunrise at the active area producing the main jet, as defined in the text.

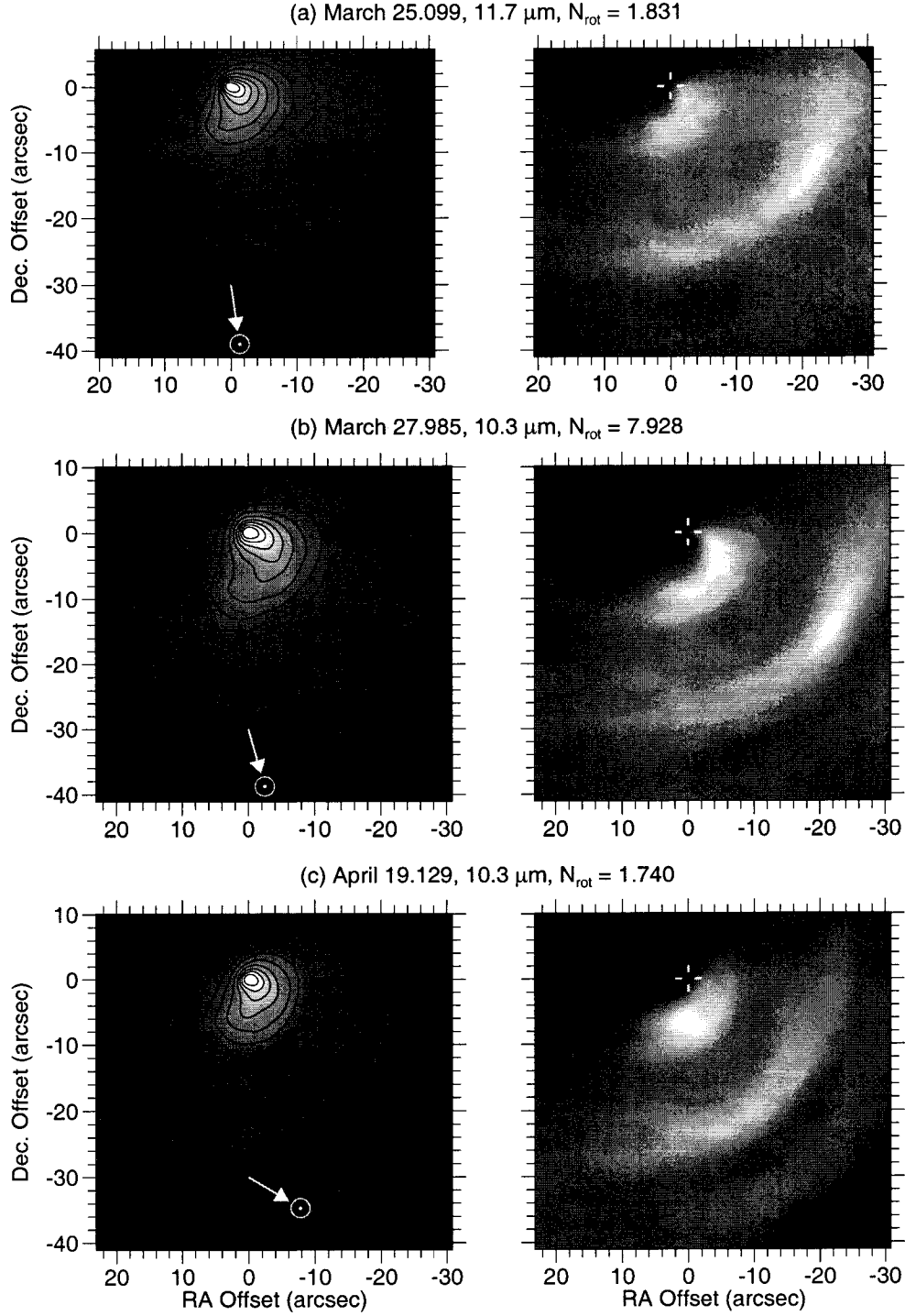


Fig. 2.— Mid-IR intensity and $1/\rho$ -divided mosaics of Hale-Bopp taken in 1997 March and April, presented as in Fig. 1. The peak isophotes are (a) 400, (b) 470, and (c) 300 Jy arcsec $^{-2}$, and the ratio between isophotes is $\sqrt{2}$. The spatial scale is about 960 km arcsec $^{-1}$ on all dates (see Table 1).

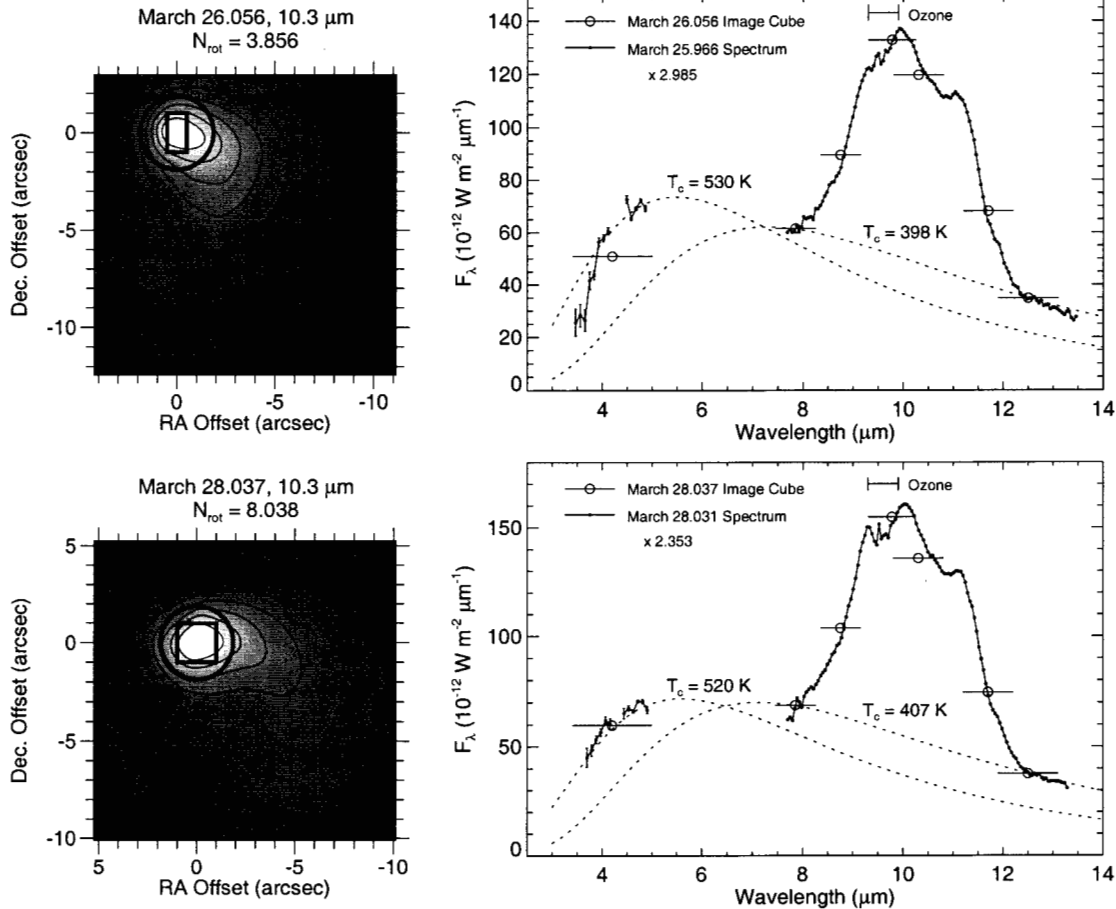


Fig. 3.— Comparisons of image cube photometry and spectral data. (Left column) Frames from the March 26.056 and March 28.037 cubes. Circles indicate the regions of the image photometry measurement, rectangles mark the positions of the spectrograph slit segment. (Right column) Image photometry (open circles), with bars that indicate the bandpass of each filter. The spectra (connected dots) have been multiplied by the indicated factors to correct for the smaller slit size and match the overall level of the photometry. The plotted blackbody curves indicate the 8–13 μm color temperature of the continuum emission which underlies the 10 μm silicate feature, and the 3–5 μm color temperature. The relative flux calibration between the 3–5 and 8–13 μm spectral segments is more accurate for March 28 (taken with a 2'' slit), than for March 26 (1'' slit). However, the narrower slit provides better calibration through the telluric ozone band near 9.5 μm .

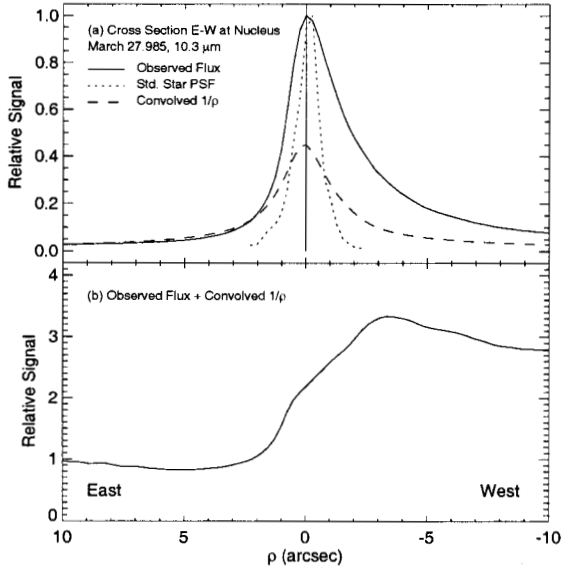


Fig. 4.— (a) East-west cross section through the intensity peak of the March 27.985 mosaic (Fig. 2b), compared to the instrumental PSF and a convolved $1/\rho$ profile. The comet cross section is much broader than the PSF, and shows no sign of an unresolved nuclear component. (b) The comet cross section divided by the convolved $1/\rho$ profile, showing the nearly flat profile to the east and the strong peak in the jet to the west.

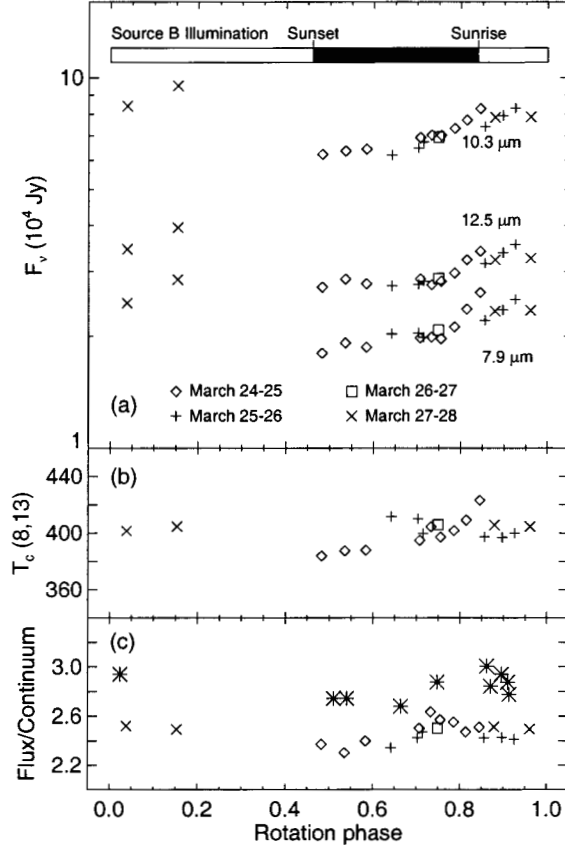


Fig. 5.— (a) Near-nucleus flux density versus rotation phase during March 24–28. The flux density was measured in $4''.3$ diameter regions centered on the intensity peak. The flux in this region varies by a factor of 1.3, and appears to be correlated with the illumination of Source B. (b, c) $T_c(8,13)$ and the silicate feature flux-to-continuum ratio derived from the three-wavelength photometry, and from the spectra in Fig. 6 (asterisks). No definite correlation with phase is detected in these parameters.

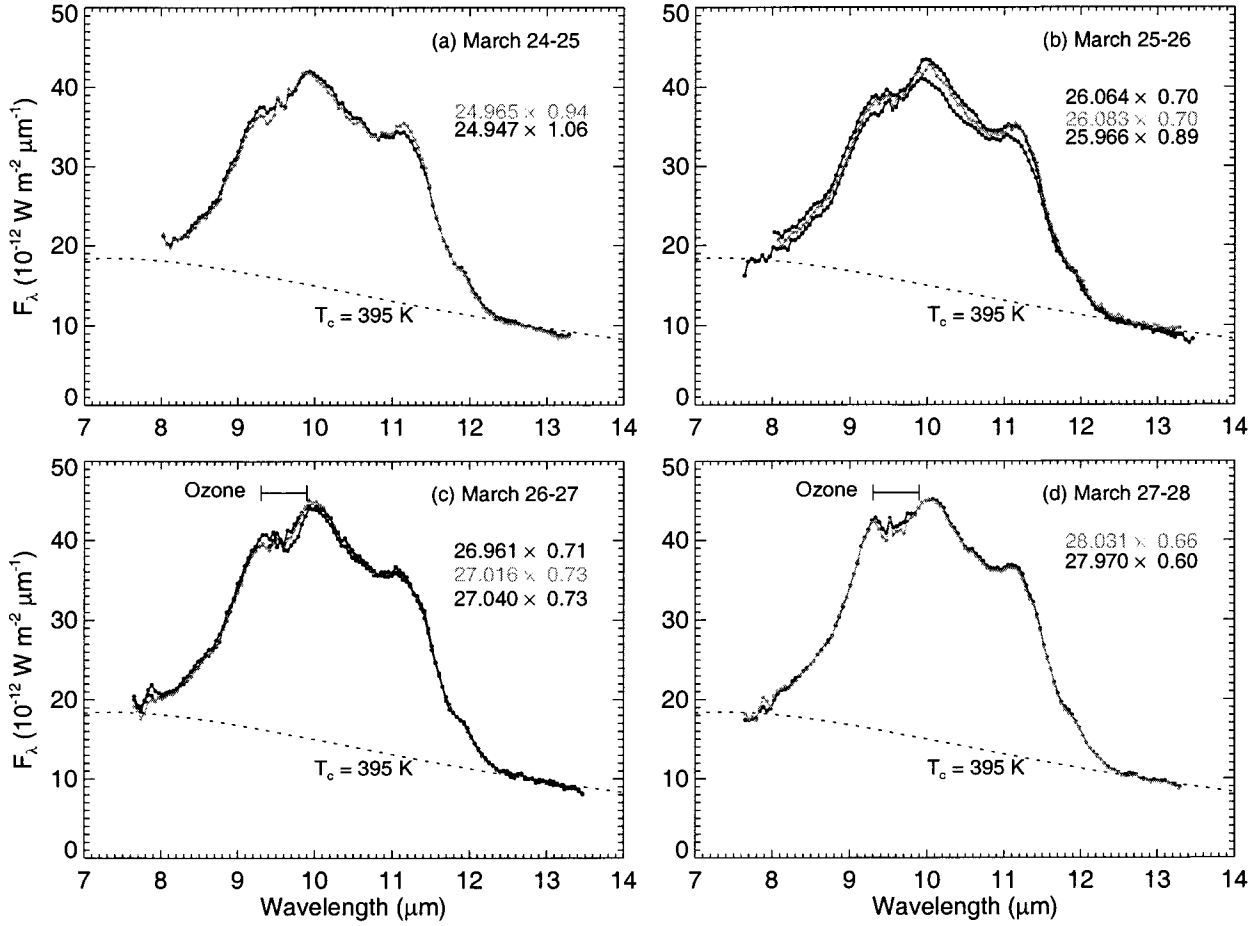


Fig. 6.— Spectra of the nuclear region from 1997 March 24–28, normalized by the indicated factors to equal 10.0 at 12.8 μm . Note that there is little variation in the silicate feature strength or shape during this time period. The 9.4 μm dip on March 27–28 is an artifact due to poor telluric ozone correction with the 2'' slit.

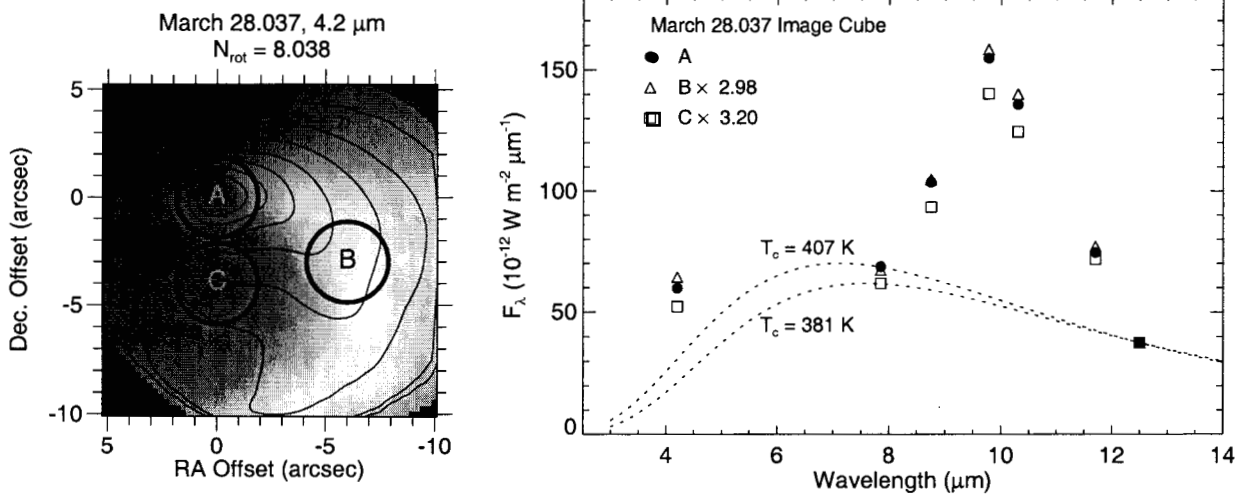


Fig. 7.— March 28.037 $1/\rho$ -divided $5 \mu\text{m}$ gray-scale image is compared to the same $10.3 \mu\text{m}$ contours as drawn in Fig. 3b. Photometry within the regions A, B, and C, scaled by the indicated factors to match at $12.5 \mu\text{m}$, shows the color temperature and silicate feature strength to be higher in the jet (region B) than at regions A and C.

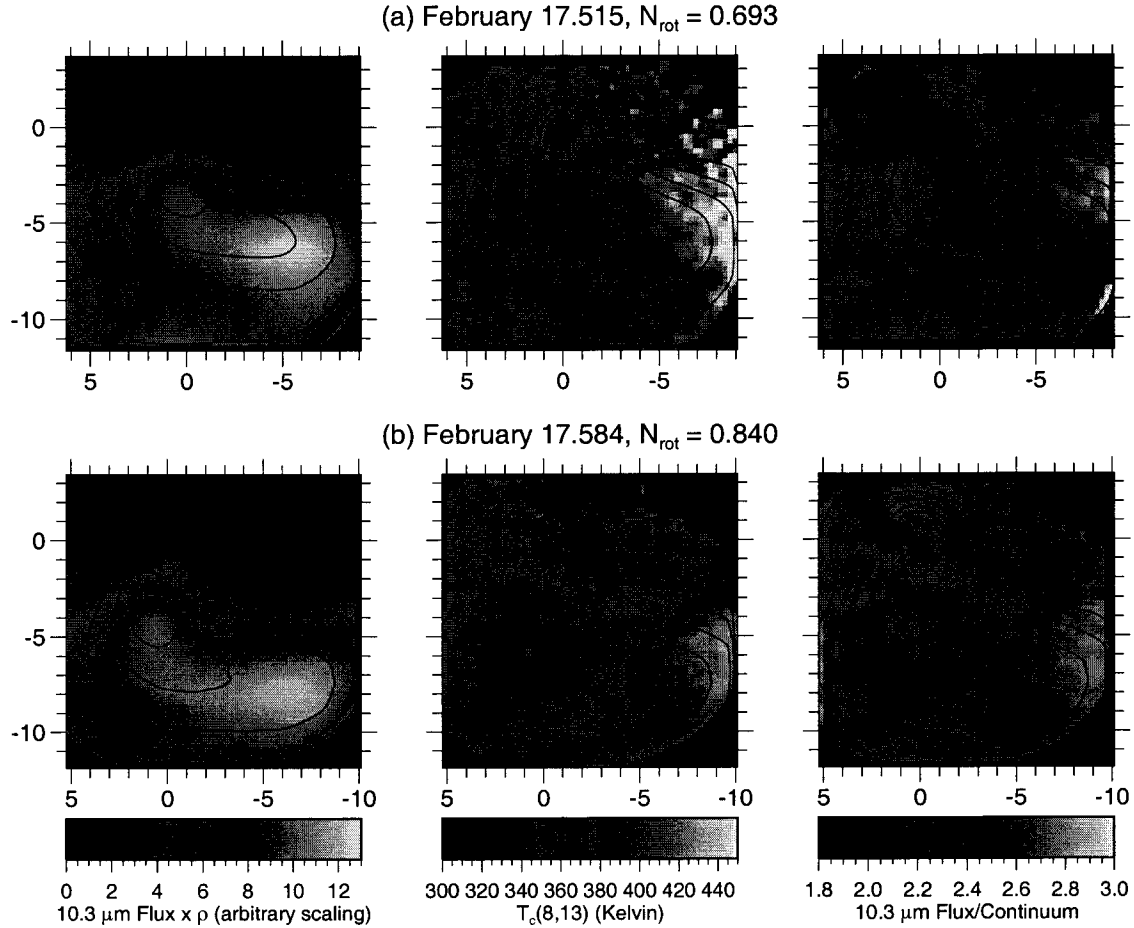
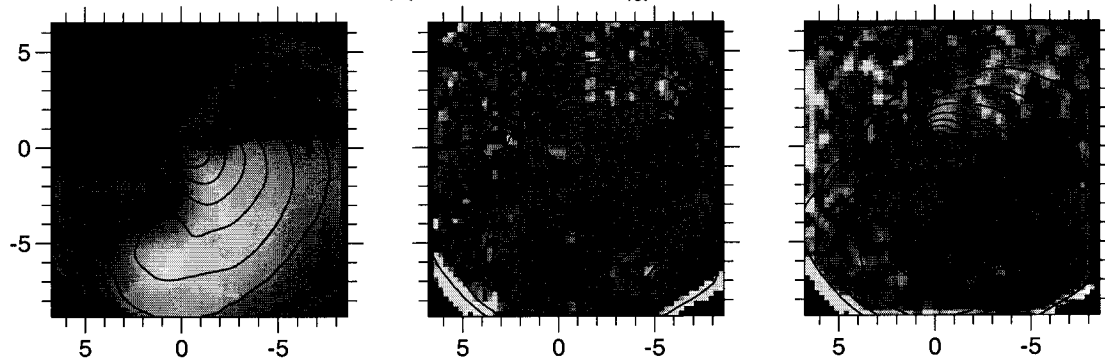
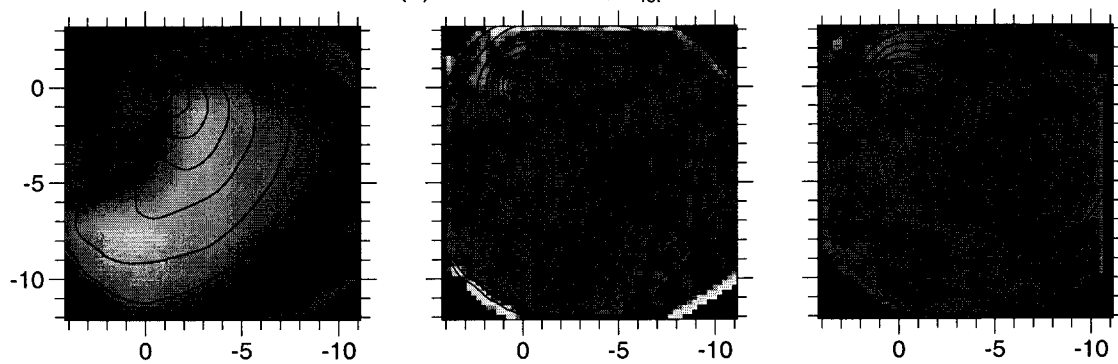


Fig. 8.— Extractions from 1997 February 17.515 and 17.584 image cubes. The isophotes in all 3 columns are from the 10.3 μm total intensity map. Colors represent (left) $1/\rho$ -divided intensity, (center) 8–13 μm color temperature, and (right) 10.3 μm flux-to-continuum ratio \mathcal{R} . The axes are labeled with the offset from the flux peak in arcsec. Note that both the color temperature and silicate feature contrast are highest in the jet, especially at the western tip.

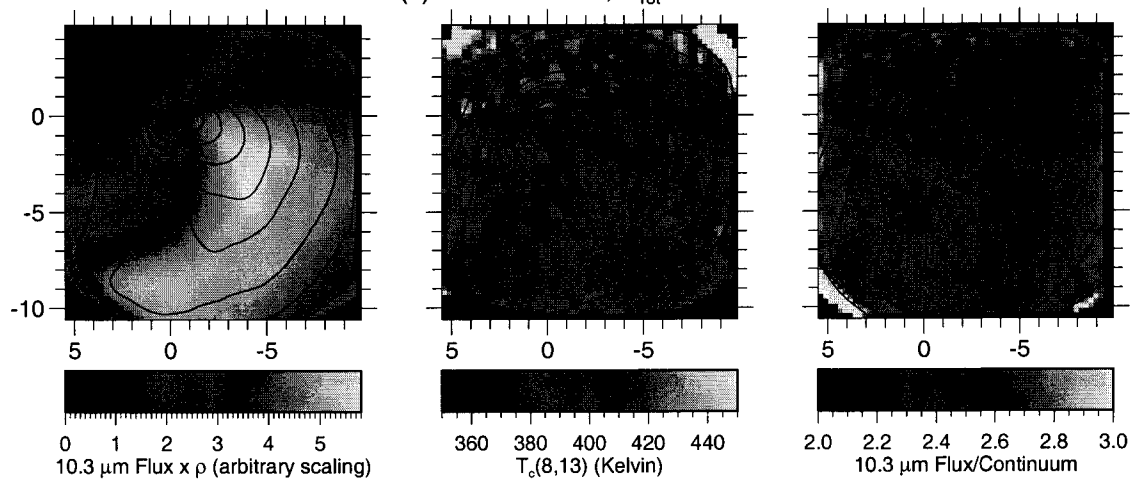
(a) March 25.078, $N_{\text{rot}} = 1.786$



(b) March 26.056, $N_{\text{rot}} = 3.856$



(c) March 26.089, $N_{\text{rot}} = 3.925$



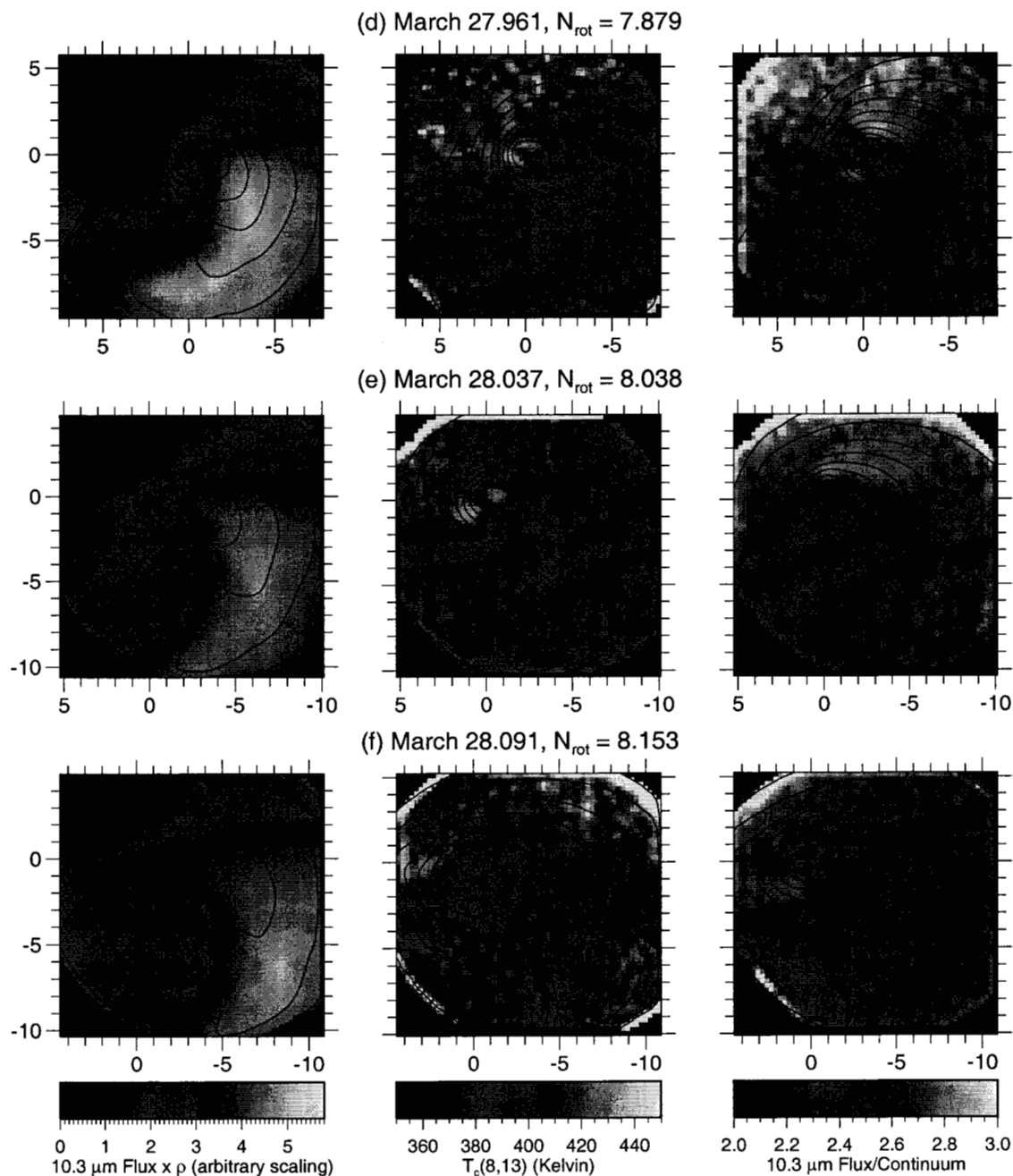


Fig. 9.— Extractions from six 1997 March image cubes, displayed as in Fig. 8. Note the steady expansion of the jet pattern as the rotation phase increases from (a) to (f). As in February, note that the color temperature and the silicate flux-to-continuum ratio peak in and slightly ahead of the jet.

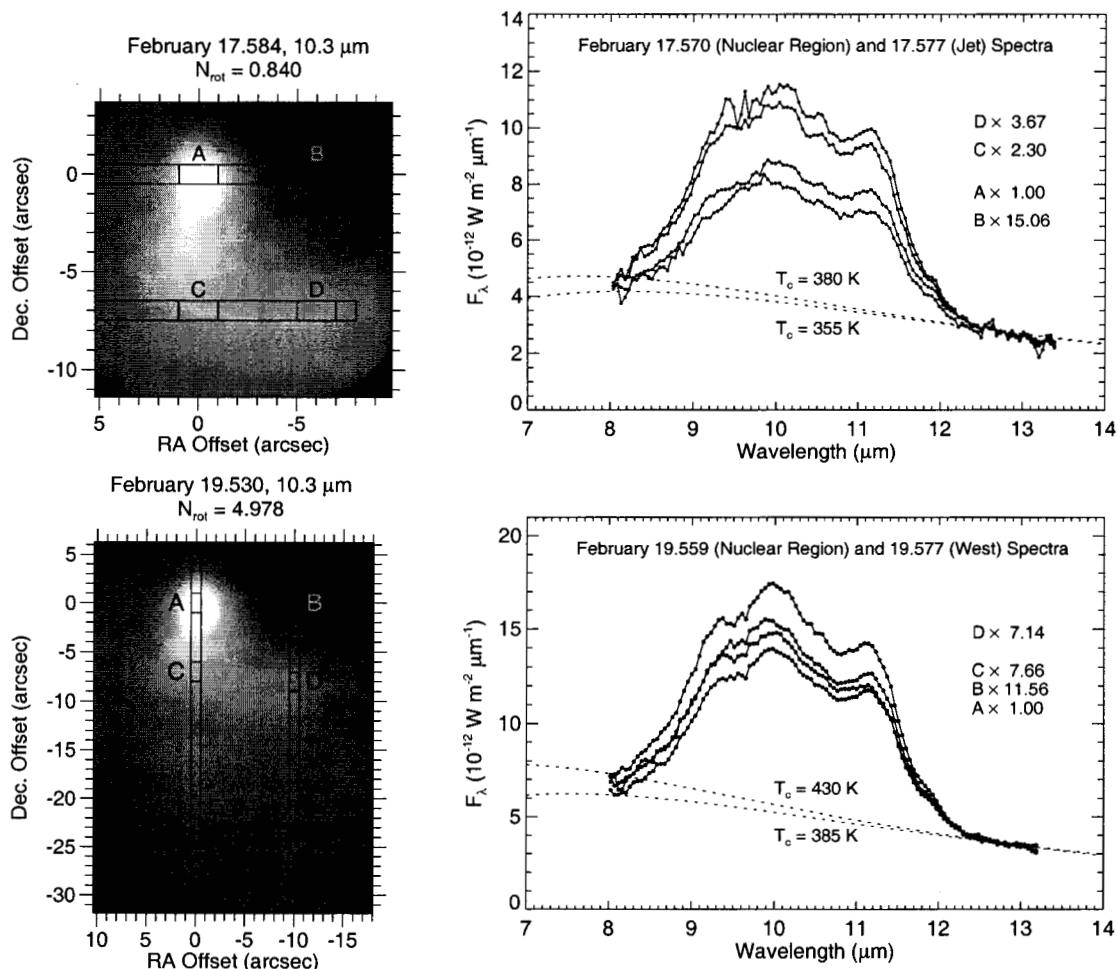


fig10b.eps: 1999 Nov 8

Fig. 10.— Variation of spectra with position in the coma on 1997 February 17 & 19. (Left) Total intensity images with overlaid rectangles marking the spectrograph slit positions. The labels A, B, C, and D identify the segments from which individual spectra were extracted. (Right) Spectra extracted from the segments. The labels show the vertical order of the plotted spectra and the scaling factors by which the data have been multiplied to match at $12.8 \mu\text{m}$. The blackbody curves indicate the color temperature of the continuum. The color temperature and the silicate flux-to-continuum ratio are highest in the jet, and their values are in good agreement with those extracted from the image cube data (Fig. 8). However, the spectral structure does not vary between the nuclear region and the jet.

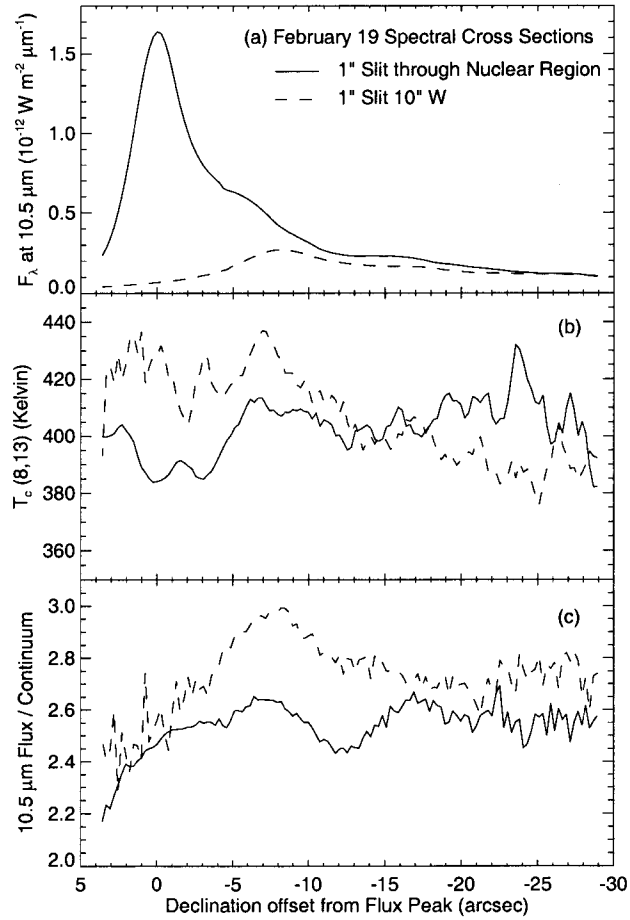


Fig. 11.— (a) The intensity at $10.5 \mu\text{m}$ along the lengths of the slits shown in Fig. 10b. (b, c) The $8\text{--}13 \mu\text{m}$ color temperature and $10.5 \mu\text{m}$ flux-to-continuum ratio along the two slits. Note that both quantities peak in the jet $\sim 7''$ S of the nucleus.

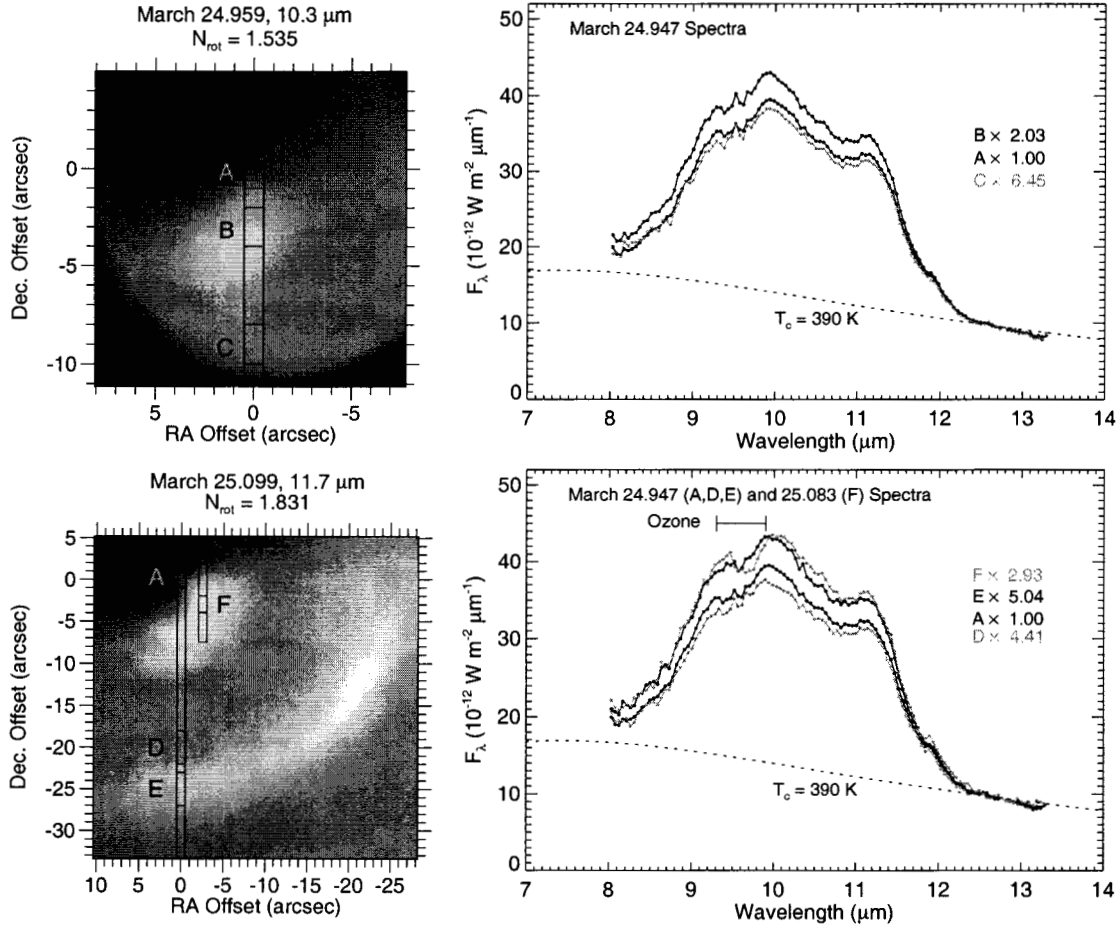


Fig. 12.— Variation of spectra with position on March 24–25, presented as in Fig. 10. The mosaic in (b) was made 3.4 h after the A–E spectrum, so segments D and E are drawn 5'' S of their true offsets to correct for the expansion during this time and indicate the segment positions relative to the halo. The color temperature and silicate flux-to-continuum ratio are highest in the jets and halos, in agreement with the images in Fig. 9. Spectra B and E, which represent dust ejected at the same phase of nuclear rotation about 2 and 13 h after ejection, are nearly identical, indicating that there is little evolution in grain properties between these times. Spectrum F was taken at high airmass and suffers from poor correction of the ozone feature near 9.4 μm .

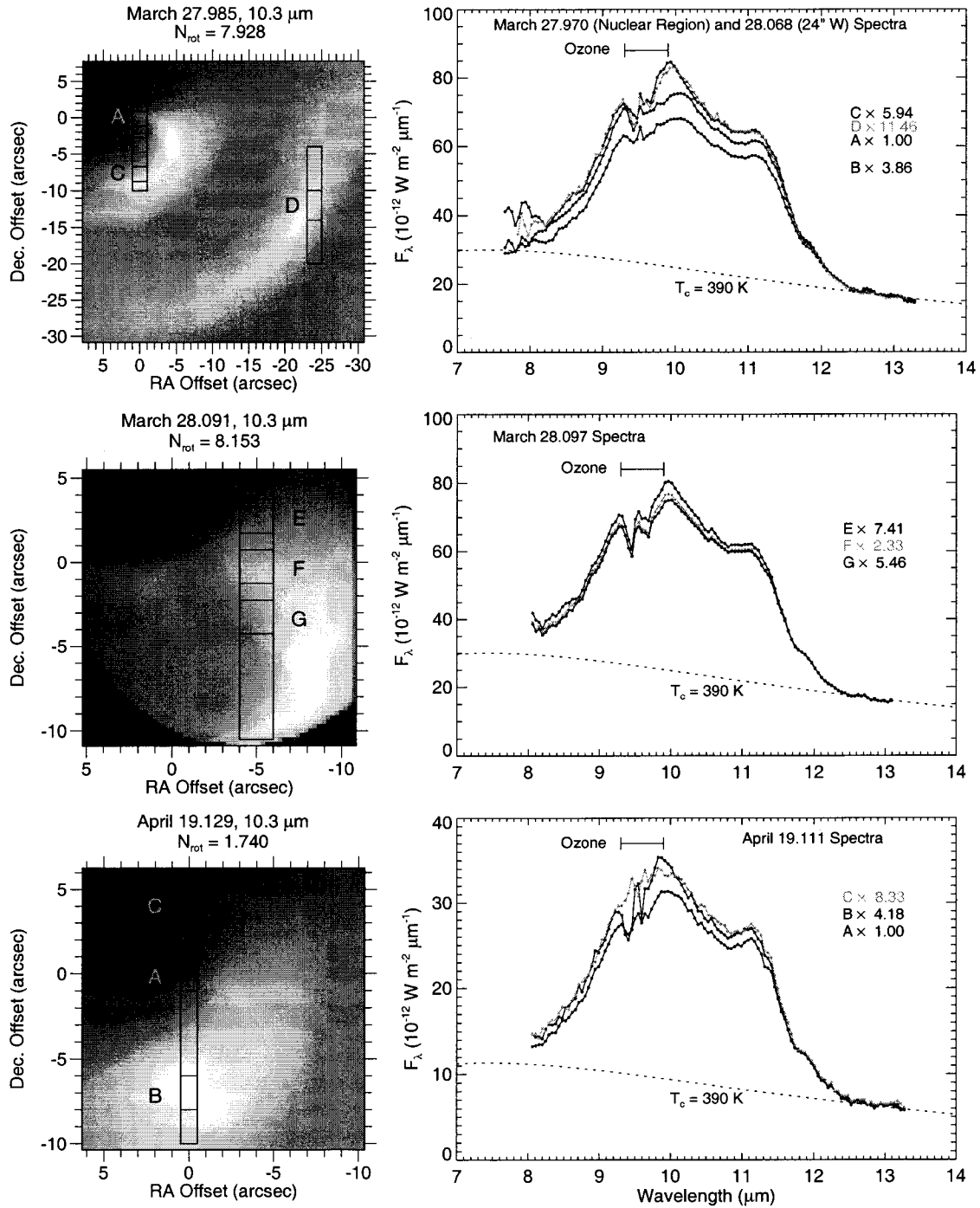


Fig. 13.— Variation of spectra with position on March 27–28 and April 19, presented as in Fig. 10. The March data were taken with the 2" slit and suffer from poor ozone correction near 9.4 μm . The silicate feature strength and color temperature are again higher in the jet and halo (C and D) than near the nucleus (A) or just behind the jet (B). Position E, to the north, shows the highest silicate feature in agreement with Fig. 9. The April 19 data also show an enhancement of the silicate feature in the jet.

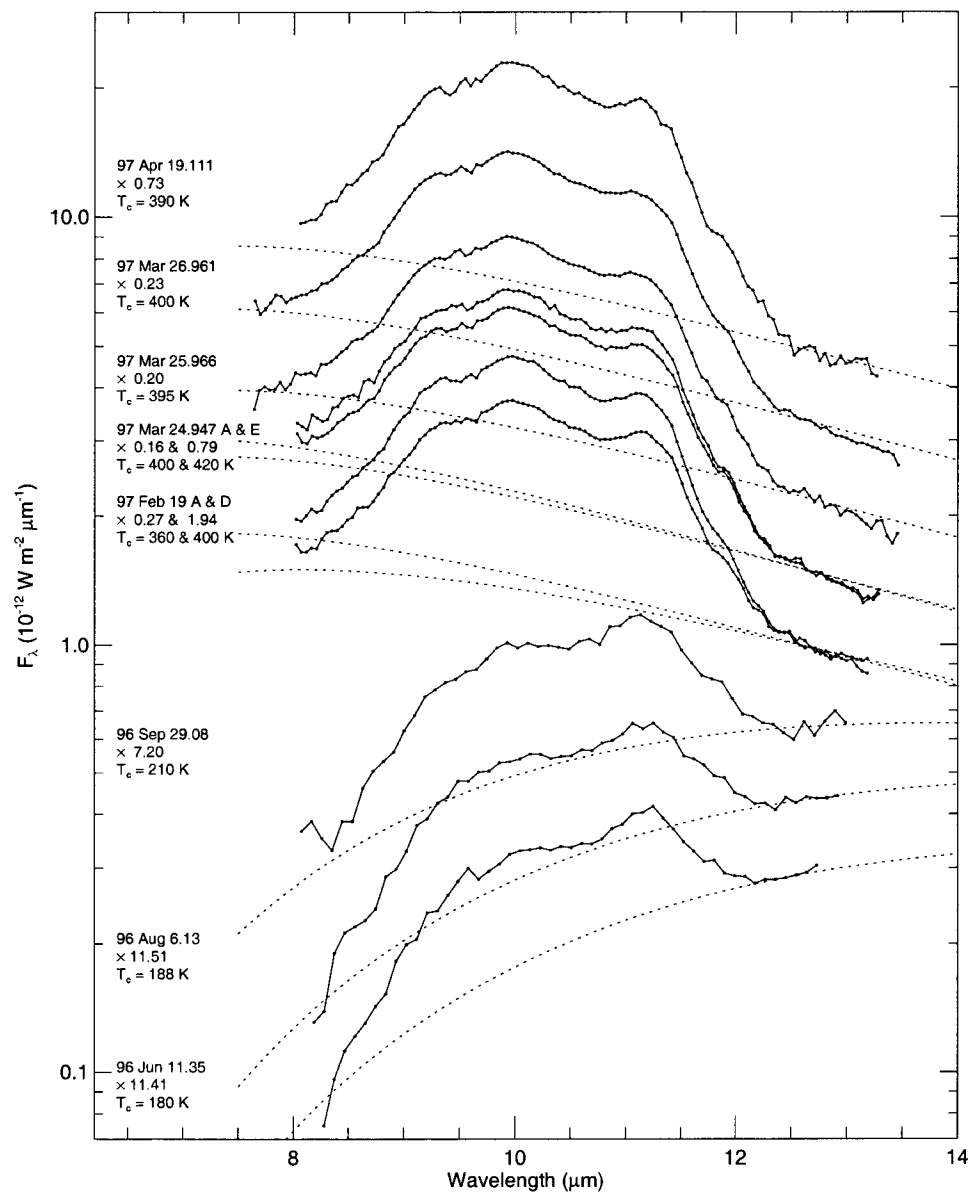


Fig. 14.— The variation in Hale-Bopp's 8–13 μ m spectrum between June 1996 and April 1997. Each spectrum has been multiplied by the indicated factor to space the curves evenly in the plot. The dotted curves indicate the blackbody continua by which the spectra were divided to produce the flux/continuum curves plotted in Fig. 15.

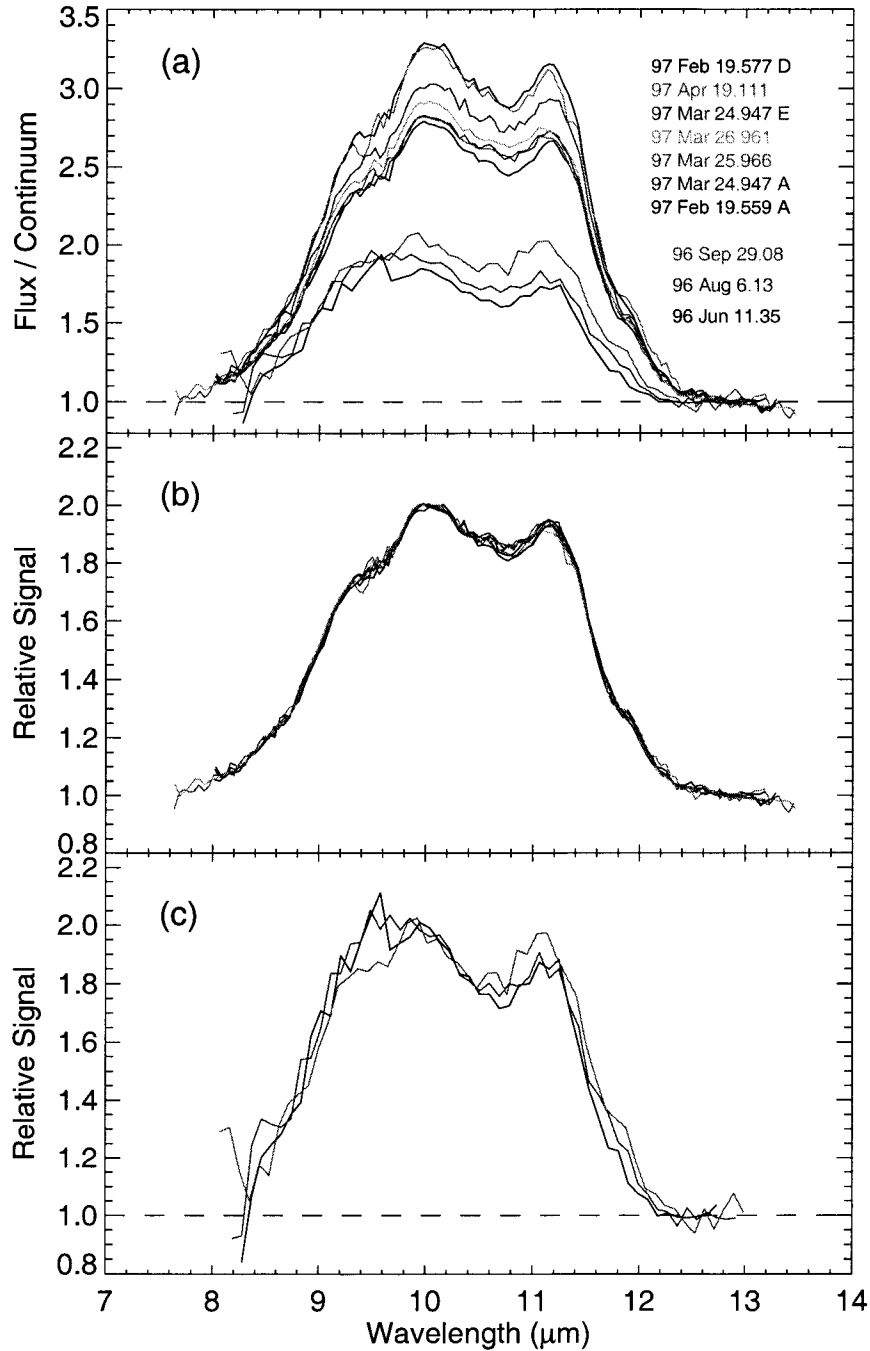


Fig. 15.— (a) The spectra from Fig. 14 divided by the blackbody curves, showing the large increase in silicate feature strength as Hale-Bopp approached perihelion. (b) The 1997 February – April flux/continuum spectra normalized to equal 2.0 at 10.0 μm . After normalization, the shapes of all the spectra are nearly identical. (c) The 1996 June – September spectra normalized in the same manner. The 10 μm peak is significantly broader in June and August than in September and near perihelion.

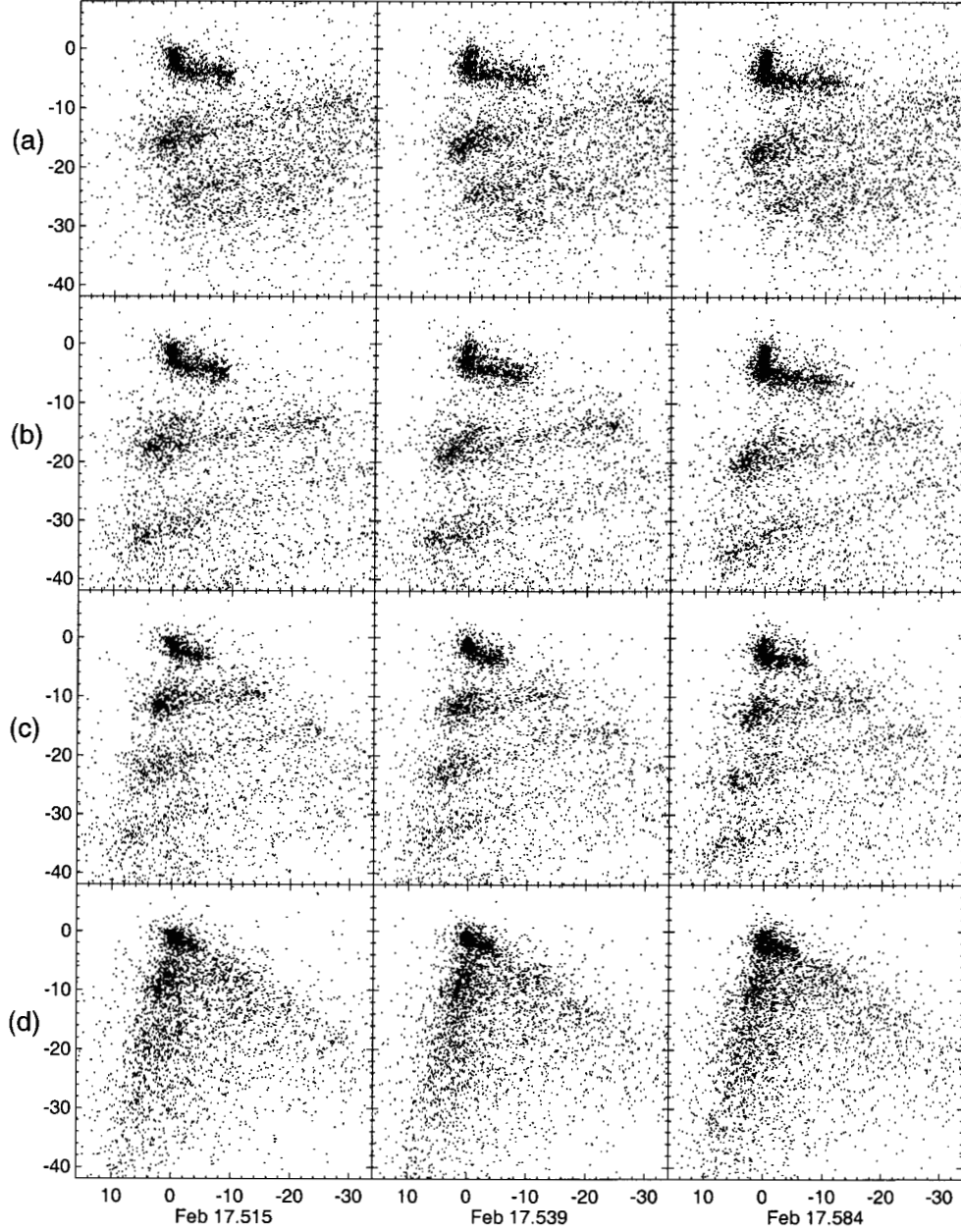


Fig. 16.— Synthetic images of Hale-Bopp’s inner dust coma on 1997 February 17. The abscissa is right ascension and the ordinate is declination, both labeled in arcsec. The sun is to the southeast, as shown in Fig. 1a. The three columns correspond to the times of the images in Figs. 1a and 8. (a) $a \approx 0.2 \mu\text{m}$ carbon grains, $\beta = 2.4\text{--}2.5$, $v_{\text{eject}} = 590 \text{ m s}^{-1}$ (b) $a \approx 0.2 \mu\text{m}$ silicate grains, $\beta = 0.6\text{--}0.7$, $v_{\text{eject}} = 558\text{--}562 \text{ m s}^{-1}$ (c) $a \approx 15 \mu\text{m}$ particles, $\beta = 0.013\text{--}0.015$, $v_{\text{eject}} = 344\text{--}354 \text{ m s}^{-1}$ (d) $a \approx 20\text{--}50 \mu\text{m}$ particles, $\beta = 0.0005\text{--}0.0100$, $v_{\text{eject}} = 120\text{--}323 \text{ m s}^{-1}$

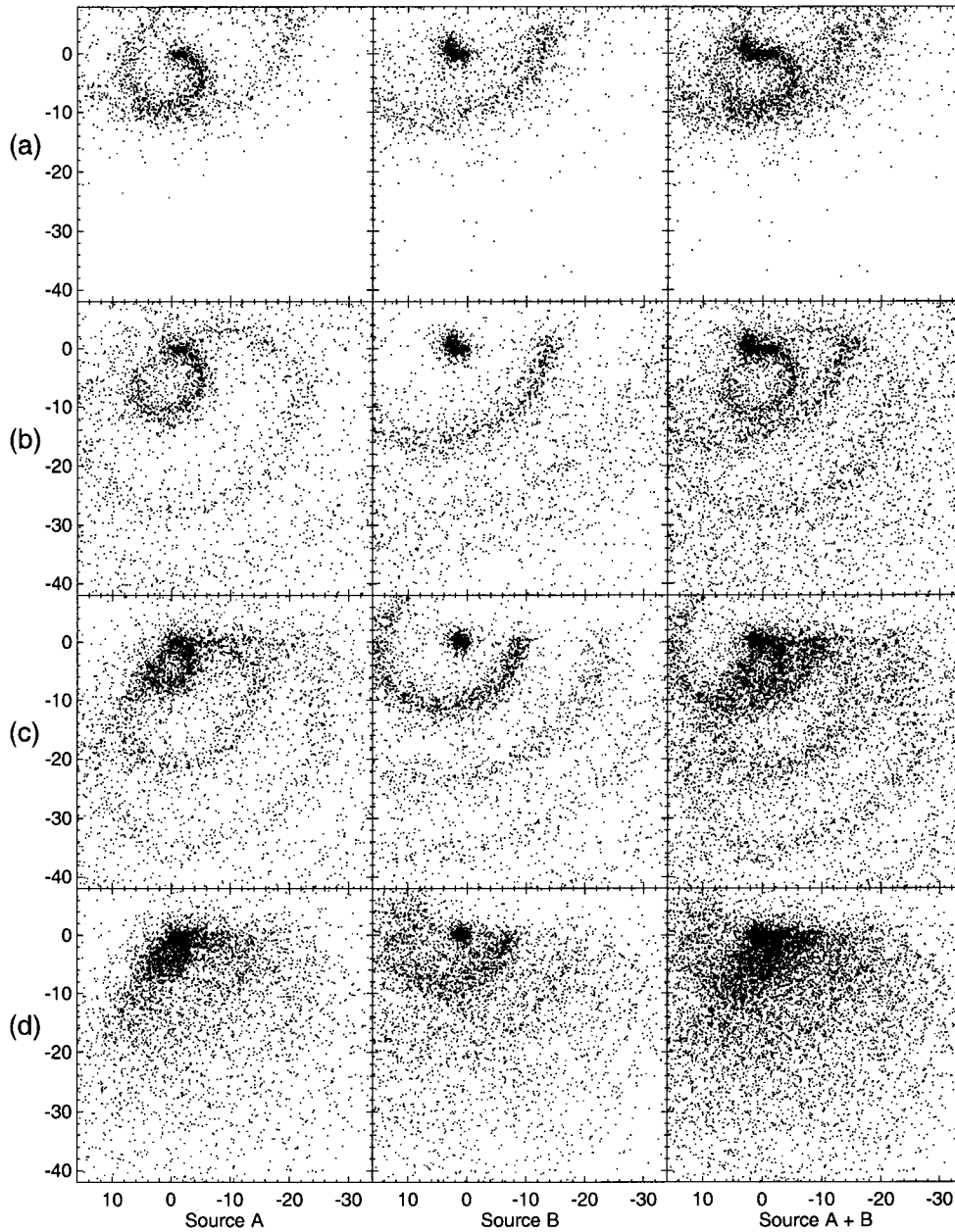


Fig. 17.— Synthetic images of Hale-Bopp’s inner dust coma on March 28.037, corresponding to Fig. 9e and 0.05 d after Fig. 2b. The images in each row incorporate the same range in β and v_{eject} as in Fig. 16. The first column displays the ejecta from Source A at $+55^\circ$ latitude and the second column the ejecta from Source B at $+5^\circ$. The third column shows the sum of the contributions from Sources A and B. The sun is to the south (Figure 2b).

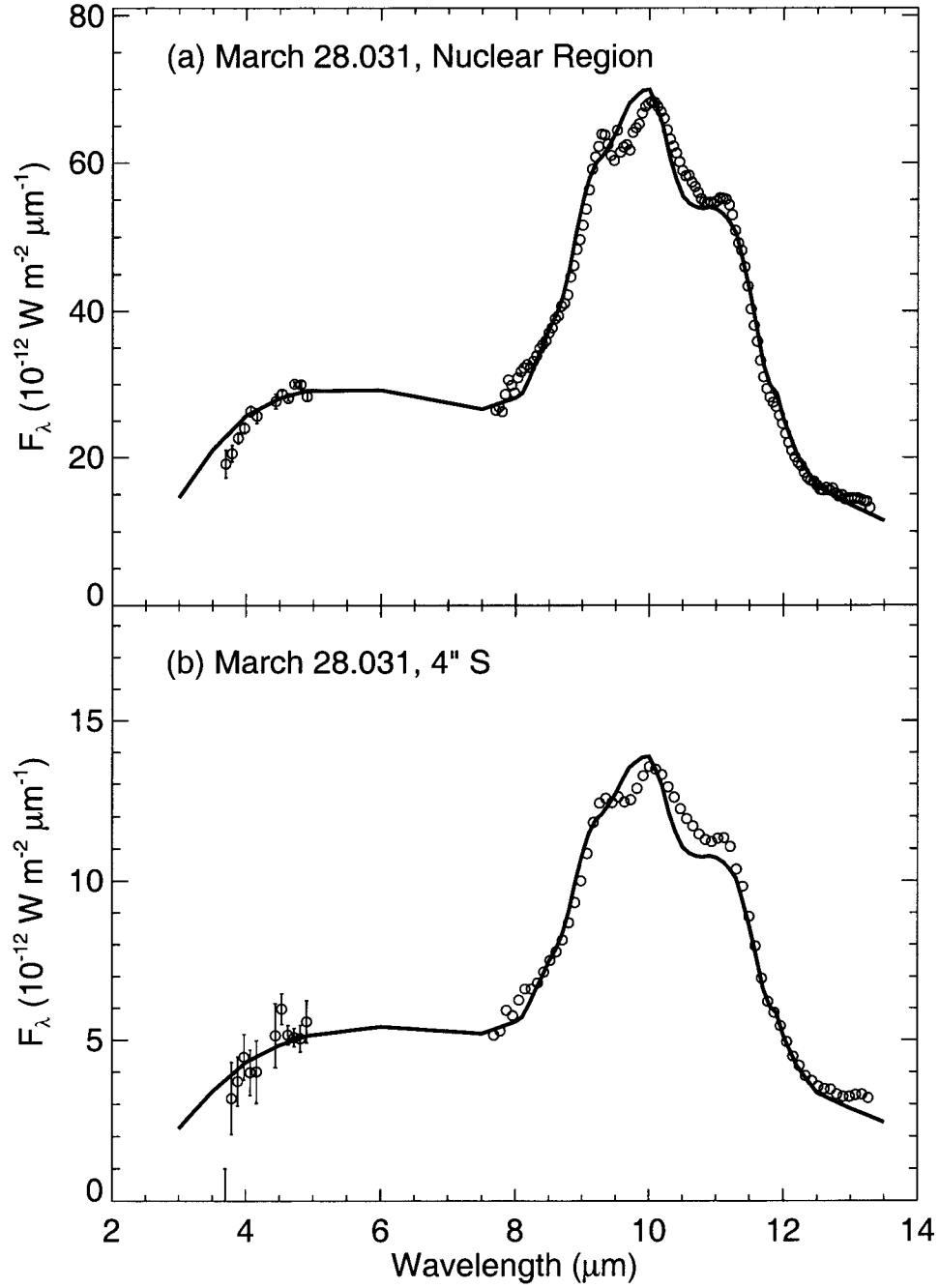


Fig. 18.— Thermal emission models fitted to the 1997 March 28.031 spectra (Figure 3b). (a) Nuclear Region ($2'' \times 2''$): size distribution parameters $a_0 = 0.05 \mu\text{m}$, $a_p = 0.13 \mu\text{m}$. (b) 4" S: $a_0 = 0.05 \mu\text{m}$, $a_p = 0.16 \mu\text{m}$.

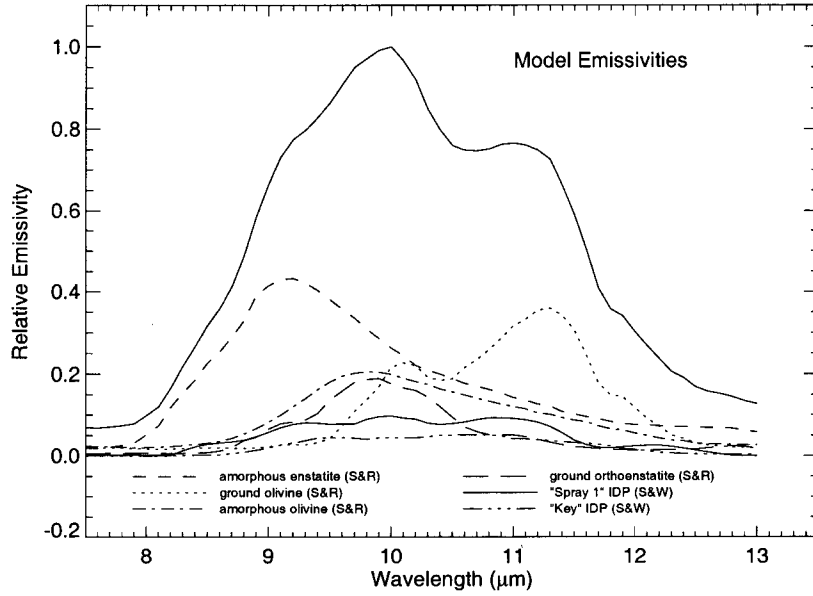


Fig. 19.— Emissivities of the silicate components used for the models. Solid line at top is the sum of the emissivity components; it is the silicate emissivity template used for fitting the spectral data. S&R: Stephens & Russell (1979); (S&W): Sanford & Walker (1985).

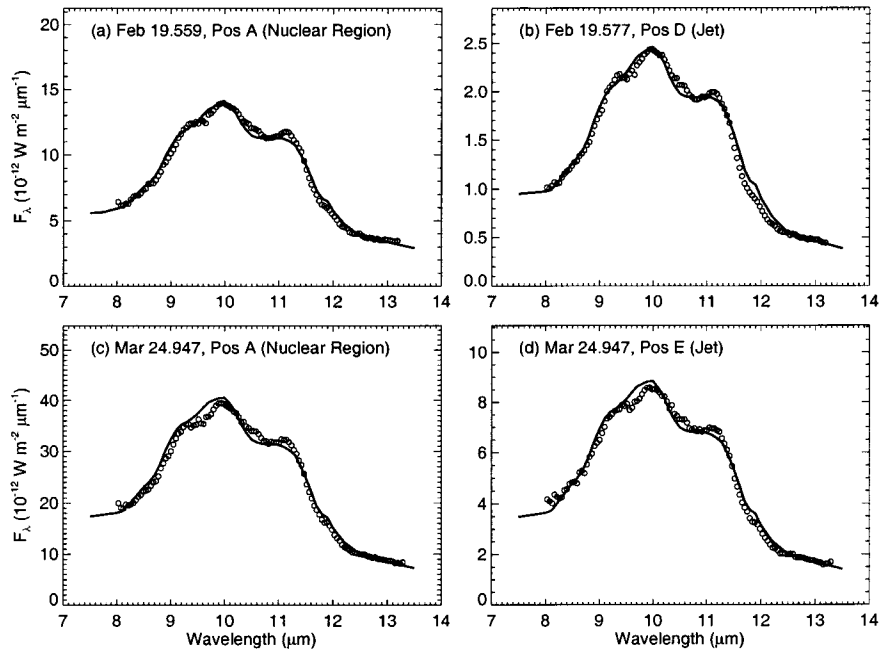


Fig. 20.— Model fits to 1997 February 19 and March 24 spectra. $a_0 = 0.05 \mu\text{m}$ for all models. The a_p values are: (a) $0.16 \mu\text{m}$; (b) $0.09 \mu\text{m}$; (c) $0.13 \mu\text{m}$; (d) $0.12 \mu\text{m}$.

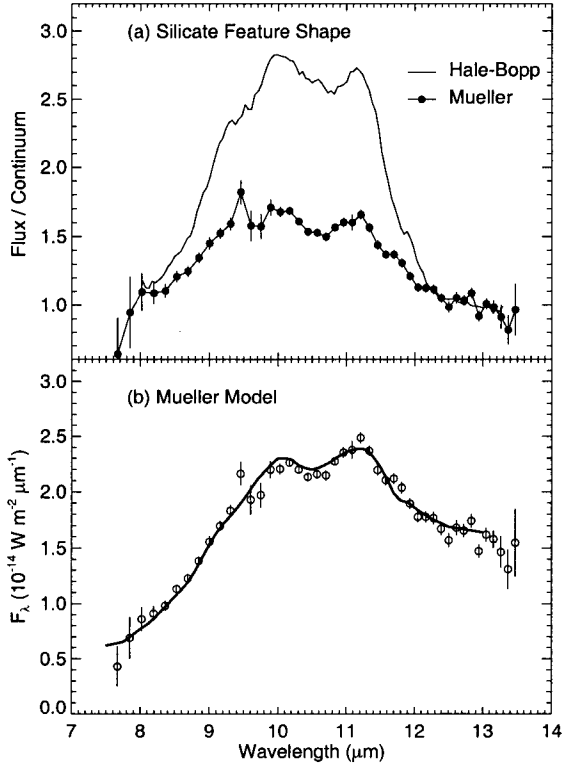


Fig. 21.— Comparison of Hale-Bopp and comet Mueller (C/1993 A1) at $r_h = 2.04$ AU. Although the silicate feature is much stronger in Hale-Bopp, the spectral structure is similar in both comets. (a) March 24.947, region A, flux/continuum spectrum compared with Mueller spectrum divided by a 220 K blackbody (Hanner et al. 1994a). (b) Comet Mueller total flux fitted with a model using the same silicate emissivity template as used for Hale-Bopp.

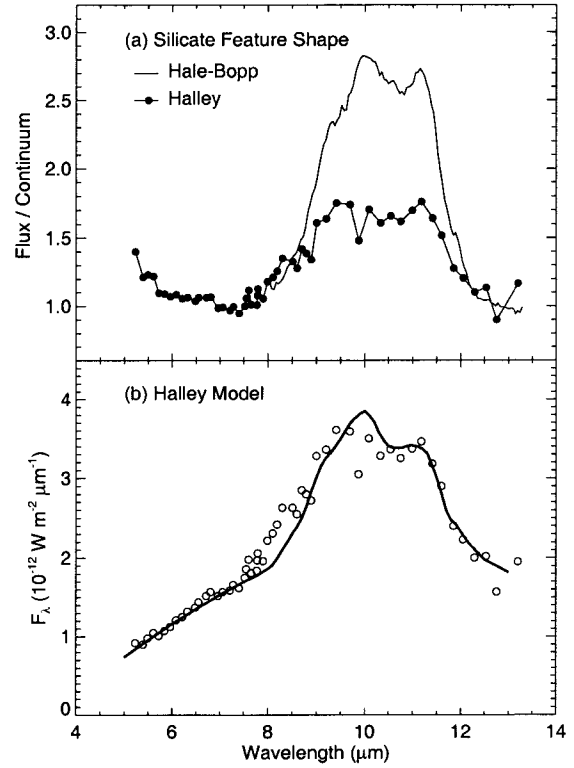


Fig. 22.— Comparison of Hale-Bopp with comet 1P/Halley at $r_h = 1.30$ AU (Bregman et al. 1987). (a) March 24.947, region A, flux/continuum spectrum compared with Halley spectrum divided by a 300 K blackbody. (b) Comet Halley total flux fitted with a model using the same silicate emissivity template as used for Hale-Bopp. Although the general spectral shape is similar, the $10 \mu\text{m}$ region is flatter in the Halley spectrum.